Journal of Power Sources 270 (2014) 221–237

Contents lists available at ScienceDirect

Journal of Power Sources

journal homepage: www.elsevier.com/locate/jpowsour

Enhancing the estimation accuracy in low state-of-charge area: A novel onboard battery model through surface state of charge determination

Minggao Ouyang*, Guangming Liu, Languang Lu, Jianqiu Li, Xuebing Han

Department of Automotive Engineering, State Key Laboratory of Automotive Safety and Energy, Tsinghua University, Beijing 100084, PR China

HIGHLIGHTS

- An extended equivalent circuit battery model (EECM) with enhanced accuracy in low state-of-charge (SOC) area is introduced.
- The EECM uses the surface SOC (SOC_{surf}) to reflect the solid-phase diffusion process.
- The low-SOC-area voltage estimation error could be reduced by more than 50% through the EECM.
- An improved SOC estimation accuracy in low-SOC area is resulted by the EECM.

ARTICLE INFO

Article history:
Received 8 May 2014
Received in revised form
14 July 2014
Accepted 15 July 2014
Available online 23 July 2014

Keywords:
Lithium-ion battery
Low state-of-charge area
Extended equivalent circuit model
Surface state of charge
Electric vehicle

ABSTRACT

In order to predict the battery remaining discharge energy in electric vehicles, an accurate onboard battery model is needed for the terminal voltage and state of charge (SOC) estimation in the whole SOC range. However, the commonly-used equivalent circuit model (ECM) provides limited accuracy in low-SOC area, which hinders the full use of battery remaining energy. To improve the low-SOC-area performance, this paper presents an extended equivalent circuit model (EECM) based on single-particle electrochemical model. In EECM, the solid-phase diffusion process is represented by the SOC difference within the electrode particle, and the terminal voltage is determined by the surface SOC (SOC_{surf}) representing the lithium concentration at the particle surface. Based on a large-format lithium-ion battery, the voltage estimation performance of ECM and EECM is compared in the entire SOC range (0–100%) under different load profiles, and the genetic algorithm is implemented in model parameterization. Results imply that the EECM could reduce the voltage error by more than 50% in low-SOC area. The SOC estimation accuracy is then discussed employing the extended Kalman filter, and the EECM also exhibits significant advantage. As a result, the EECM is very potential for real-time applications to enhance the voltage and SOC estimation precision especially for low-SOC cases.

© 2014 Elsevier B.V. All rights reserved.

1. Introduction

Due to the excellent performance in driving economy and environmental friendliness, electric vehicles (EVs) have attracted significant attention, especially for the pure electric vehicles (PEVs) with zero-emission capability. However, the PEV driving range is not competitive compared with the range of conventional vehicles owing to the low energy density and high cost of vehicle battery, which is one of the key drawbacks from the view of the potential EV consumers [1]. Additionally, the estimation error of PEV remaining driving range (RDR) could not be neglected owing to the inaccuracy of battery state estimation and brings considerable range anxiety to the passengers [2]. An accurate RDR depends on the precise estimation of battery remaining discharge energy (E_{RDE}), which relies on an accurate battery model to calculate the terminal voltage (U_t) and the state of charge (SOC). As in Eq. (1), the remaining discharge energy (E_{RDE}) could be calculated by the future average terminal voltage ($U_{t,avg}$), the current SOC, and the permitted lower SOC limit ($SOC_{lim,l}$) to prevent overdischarge, in which I is the future current input and Q_{st} is the battery standard capacity [3]. The $SOC_{lim,l}$ is determined by the onboard battery management strategy considering SOC estimation error.

* Corresponding author. Tel.: +86 10 62792797; fax: +86 10 62789699.
E-mail addresses: ouymg@tsinghua.edu.cn (M. Ouyang), lgm06@mails.tsinghua.edu.cn (G. Liu).

http://dx.doi.org/10.1016/j.jpowsour.2014.07.090
0378-7753/© 2014 Elsevier B.V. All rights reserved.

$$E_{\mathrm{RDE}} = \int_{\mathrm{SOC}}^{\mathrm{SOC}_{\mathrm{lim},l}} U_{\mathrm{t,avg}} \cdot I \cdot \mathrm{d}t = \int_{\mathrm{SOC}}^{\mathrm{SOC}_{\mathrm{lim},l}} U_{\mathrm{t,avg}} \cdot Q_{\mathrm{st}} \cdot \mathrm{dSOC} = Q_{\mathrm{st}} \cdot U_{\mathrm{t,avg}} \cdot (\mathrm{SOC} - \mathrm{SOC}_{\mathrm{lim},l}) \quad (1)$$

Lithium-ion battery is one of the best candidates for PEV energy storage system for its high energy density and cycling lifetime, and a plenty of real-time modeling efforts have been made [4–13]. However, since the Li-ion battery shows strong nonlinearity in low-SOC area (e.g. at SOC lower than 20%), the present onboard models could hardly provide satisfying SOC and voltage results in low-SOC range, and an overestimation of SOC could lead to battery energy exhaustion before expectation and force the PEV into limp-home status. As a result, a certain part of battery energy needs to be reserved in real-world applications by technically setting a relatively large $\mathrm{SOC}_{\mathrm{lim},l}$ (normally larger than 10%) [14,15]. The battery energy could hence not be fully implemented and the PEV driving range is further restricted. If the battery model accuracy in low-SOC area is raised, a smaller $\mathrm{SOC}_{\mathrm{lim},l}$ value could be used and more battery energy could hence be utilized to obtain a larger driving range without battery cost increase. To our knowledge, the low-SOC-area model accuracy is seldom discussed in existing publications.

There exist a number of studies on lithium-ion battery models, in which the main work lies in equivalent circuit models [6–13], electrochemical models [16–18], and the impedance model [19,20]. The equivalent circuit model (ECM) reflects the battery performance by an electrical circuit composed of a set of basic electric components (resistors, capacitors, inductors, etc.), through which the voltage response under a certain current input is calculated. The model structure is mostly empirical based and the parameters are determined through battery discharging/charging experiments. Due to its low computational complexity and low difficulty in parameterization process, the ECM is frequently employed in onboard state estimation cases. The most commonly used ECM consists of a pure resistor and several resistor-capacitor parallel circuits (RC components), such as the one-state ECM with one RC component [7,8] and the two-state ECM with two RC components [9–13], etc. Generally, more RC components in the ECM lead to improved voltage and SOC estimation accuracy at the cost of larger calculation amount, and many researchers implemented the two-state ECM as a balanced choice to validate the performance of their battery state estimators. According to the literature, the ECM could provide relatively satisfying voltage and SOC results in high and middle SOC area, but the model accuracy in low-SOC area was seldom mentioned. The lowest SOC value was usually determined not less than 10% in experimental validation, e.g. 40% by Hu et al. [4], 25% by Lin et al. [9], 20% by He et al. [6], and 10% by Xiong et al. [8]. From our experience and some of the literature results [13,19], the precision of the traditional ECM usually becomes worse at SOC lower than 20% and decreases evidently under 10% SOC. As a result, the model inaccuracy at low SOC hinders the ECM performance in onboard E_{RDE} estimation, which requires high model accuracy in the whole SOC range.

The electrochemistry-based battery model is another focus of the present research, in which terminal voltage and SOC are determined based on the porous electrode structure and the electrochemical reaction process, and a better understanding of the electrochemical mechanism is provided compared with the equivalent circuit models. A large number of studies in this topic are based on the electrochemical pseudo-two-dimensional model (P2DM) developed by Doyle et al. [16] to describe the battery macroscopic behavior during operation. In Doyle's model, the cell is divided into two dimensions (i.e. the macroscopic electrode-separator dimension and the microscopic particle dimension) and the terminal voltage U_{t} is calculated through numerical method by five partial differential equations. The large calculation load caused by the numerical computation makes the P2DM hardly accessible in onboard cases. A series of model simplification attempts were made through different assumptions and approximations to reduce the computational complexity, and the resulted models were combined with real-time estimation methods e.g. Kalman filtering to provide voltage and SOC estimation results. By assuming the current density distribution within one electrode as uniform and neglecting the spatial difference in liquid-phase potential and liquid-phase lithium concentration, Santhanagopalan et al. [18] came out with the single-particle model (SPM) and proved its accuracy under constant-current discharge profile. Based on Santhanagopalan's SPM, Domenico et al. [21] considered the liquid-phase potential distribution, Prada et al. [22] and Luo et al. [23] discussed the influence of liquid-phase concentration distribution, and the double layer effect was mentioned in Marcicki's model [24]. The SPMs present accurate results in voltage and SOC estimation in the whole SOC range, but the increase of computational load is still not negligible compared with the ECM, and the battery electrochemical parameters could hardly be precisely determined by automotive engineers. Consequently, the electrochemical model needs more simplification for real-world PEV applications.

In addition, some battery models are based on the electrochemical impedance spectroscopy (EIS) method, through which a relatively complex equivalent circuit model (or so-called impedance model) is resulted. Andre et al. [19] developed an impedance model from EIS results, in which two constant phase elements (CPEs) and a Warburg component are implemented to meet the requirements in different current frequencies. Li et al. [20] took account of the electrolyte resistance, the impedance of solid-electrolyte interface (SEI), the double layer effect, and the solid-phase diffusion, and presented a complex electrochemical impedance model which perfectly agreed with the EIS experimental results. The impedance model provides better estimation results than the ECM in a wide frequency range, but the implementation of complex electrical components (e.g. the CPE and the Warburg element) makes it impossible to transfer the model parameters from the frequency domain into the time domain directly, and the impedance model is hence difficult to be expressed in an iterative form for real-time cases. Similar to the ECM, the impedance model also encounters problems in low-SOC-area performance [19].

The general characteristics of the ECM, the electrochemical model, and the impedance model are summarized in Table 1. As the only model type suitable for real-time cases, the ECM is chosen as the basis of model modification to improve the low-SOC-area performance.

This paper aims at developing a real-time-applicable battery model with enhanced estimation accuracy in low-SOC area, through which more energy stored in the battery could be used for EV drive. Based on the single-particle electrochemical model, this research presents the extended equivalent circuit model (EECM), in which the surface SOC ($\mathrm{SOC}_{\mathrm{surf}}$) representing the lithium concentration at

Table 1
Comparison of different types of lithium-ion battery models.

Model structure	Model accuracy in low-SOC area	Calibration effort	Availability in onboard cases
Equivalent circuit model	Poor	Low	Good
Electrochemical model	Good	High	Poor
Impedance model	Poor	Relatively low	Relatively poor

electrode particle surface is determined to describe the solid-phase diffusion process. The EECM shows good nonlinear performance with the help of the SOC_{surf} term and could follow the voltage fluctuation in the entire SOC range very well. A type of large-format lithium-ion battery was employed for experimental validation, and the EECM tends out to provide largely-improved performance in low-SOC area compared with the commonly-used ECM. The remainder of this paper is structured as follows. Section 2 derives the extended equivalent circuit battery model based on the simplification of single-particle model, and the advantage of the EECM in low-SOC area is theoretically explained. Section 3 explains the experimental setup and the parameter identification process. The model validation and comparison are discussed in detail in Section 4, and Section 5 shows the real-time SOC estimation results through extended Kalman filter. Section 6 concludes this paper.

2. Battery extended equivalent circuit model

2.1. Simplified explanation of battery voltage response based on single-particle model

From the electrochemical viewpoint, the operating process of lithium-ion battery is explained as the lithium intercalation/deintercalation in electrode particles and the movement in electrolyte between negative and positive electrodes. The purpose of this research is to obtain a real-time-realizable battery model through simplification of the original electrochemical understandings, and the single-particle model (SPM) is hence employed as the basis of the following discussion. The SPM treats the size and dynamics of the electrode particles as well as the current density as identical within an electrode, and the negative and positive electrodes could consequently be seen as two electrode particles. As in Eq. (2), the battery open circuit voltage (U_{OCV}) is related to the positive electrode potential $U_p(c_{b,p})$ and negative electrode potential $U_n(c_{b,n})$, which depends separately on the bulk average lithium concentration of the positive and negative electrode particles ($c_{b,p}$ and $c_{b,n}$). Note that the variables related to lithium concentration in this work indicate the solid-phase concentration without special statements. The terminal voltage U_t is more directly reflected by the lithium concentration at the particle surface ($c_{surf,p}$ and $c_{surf,n}$), i.e. the positive electrode surface potential $U_p(c_{surf,p})$ and the negative electrode surface potential $U_n(c_{surf,n})$, in which the potential subtraction is noted as ΔU_{surf} in Eq. (3). The general relationship of ΔU_{surf} and U_{OCV} during operation could be explained by Eq. (4). When the battery is after a long-time rest, the particle surface concentration equals the bulk average concentration ($c_{b,p}$ and $c_{b,n}$) and ΔU_{surf} equals U_{OCV}.

$$U_{OCV} = U_p\left(c_{b,p}\right) - U_n\left(c_{b,n}\right) \tag{2}$$

$$\Delta U_{surf} = U_p\left(c_{surf,p}\right) - U_n\left(c_{surf,n}\right) \tag{3}$$

$$\Delta U_{surf} = U_{OCV} + \left(U_p\left(c_{surf,p}\right) - U_p\left(c_{b,p}\right)\right) + \left(U_n\left(c_{surf,n}\right) - U_n\left(c_{b,n}\right)\right) \tag{4}$$

The battery discharge process is explained in Fig. 1. Here we mainly consider the lithium-ion battery with carbon-based

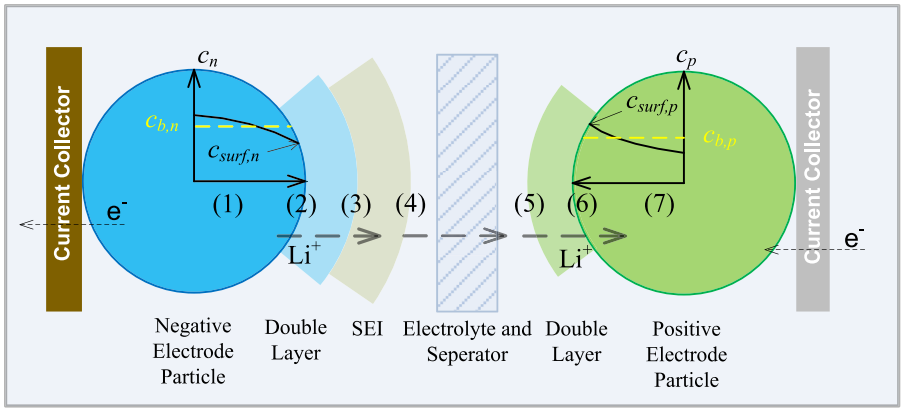

(1)→(2): Solid-phase diffusion in negative electrode particle
Voltage change: $U_n(c_{surf,n})$-$U_n(c_{b,n})$
(2)→(3): Charge transfer in double layer (anode)
Voltage change: $U_{DL,n}$
(3)→(4): Current flow through SEI film
Voltage change: U_{SEI}
(4)→(5): Current flow through seperator and diffusion in electrolyte
Voltage change: U_0, U_{ED}
(5)→(6): Charge transfer in double layer (cathode)
Voltage change: $U_{DL,p}$
(6)→(7): Solid-phase diffusion in positive electrode particle
Voltage change: $U_p(c_{surf,p})$-$U_n(c_{b,p})$

Fig. 1. Explanation of lithium-ion battery discharge process based on single-particle model.

negative electrode, in which the solid-electrolyte interface (SEI) film on the anode surface needs consideration. Lithium diffuses in anode particle to the particle surface where the charge transfer occurs, moves through the SEI film into electrolyte [25], flows in the liquid phase through the separator to the cathode charge-transfer interface, intercalates into the cathode particle, and starts the cathode solid-phase diffusion. Each procedure results in a corresponded voltage change, which makes the battery terminal voltage deviating from U_{OCV}. The difference between surface concentration c_{surf} and bulk concentration c_b indicating the solid-phase diffusion results in the gap between ΔU_{surf} and U_{OCV} ($U_n(c_{surf,n})$-$U_n(c_{b,n})$ and $U_p(c_{surf,p})$-$U_p(c_{b,p})$, noted later as $U_{SD,n}$ and $U_{SD,p}$), and the double layer effect in anode and cathode leads to the voltage changes $U_{DL,n}$ and $U_{DL,p}$. The voltage drops U_{SEI} and U_0 are caused by the current flow through the SEI film and the electrolyte, and the effect of contact resistance and current collector resistance is also combined in U_0 for convenience. U_{ED} represents the voltage drop owing to liquid-phase diffusion. The battery voltage output could then be expressed in Eq. (5). It is noticed that the voltage change in SEI film is a high-frequency term with the time constant lower than 0.1 s [20], and the film could be seen as a pure resistor for the low-frequency EV driving conditions, in which U_{SEI} is merged with U_0. The voltage changes on the double layer capacitance ($U_{DL,n}$ and $U_{DL,p}$) are later analyzed as transient processes. The voltage drop caused by electrolyte diffusion needs to be considered only under very high current rate and could only be well calculated by more than seven parameters [23], which largely raise the model complexity. The term U_{ED} is consequently here neglected and the terminal voltage could be written as Eq. (6).

$$U_t = U_{OCV} - U_{SD,n} - U_{SD,p} - U_0 - U_{SEI} - U_{DL,n} - U_{DL,p} - U_{ED} \tag{5}$$

$$U_t = U_{OCV} - U_{SD,n} - U_{SD,p} - U_0 - U_{DL,n} - U_{DL,p} \tag{6}$$

According to the SPM, the battery state of charge (SOC) is represented by the average bulk concentration in the electrode particle (c_b). For the negative electrode, the bulk concentration when the battery is full (SOC equals 100%) is noted as $c_{b,n,100\%}$, and the concentration for an empty battery (SOC equals 0%) is written as $c_{b,n,0\%}$. As a result, the present SOC could be calculated by $c_{b,n}$ or the positive electrode concentration $c_{b,p}$ as in Eq. (7), and the open circuit voltage U_{OCV} is hence related to the macroscopic SOC.

$$SOC = \frac{c_{b,n} - c_{b,n,0\%}}{c_{b,n,100\%} - c_{b,n,0\%}} = \frac{c_{b,p} - c_{b,p,0\%}}{c_{b,p,100\%} - c_{b,p,0\%}} \tag{7}$$

Known from Eqs. (4) and (6), U_t and ΔU_{surf} are more directly related to the surface concentration c_{surf} rather than the bulk concentration c_b indicating macroscopic SOC, and the implementation of SOC could not reflect the battery dynamics straightly. Here we define the term surface state of charge (SOC_{surf}) to reflect the particle surface lithium concentration in Eq. (8). The surface SOCs of anode and cathode are in direct relation to the present potentials at the surface of positive and negative electrodes, and the terminal voltage could consequently be represented by SOC_{surf} in Eq. (9). For the battery management system (BMS) developers without specific electrochemical techniques, separate calibration of the negative and positive electrode potentials is very inconvenient. To make our presented model more suitable for real-world applications, a single SOC_{surf}-potential curve is used to approximate the subtraction of positive surface potential $U_p(SOC_{surf,p})$ and negative surface potential $U_n(SOC_{surf,n})$, i.e. ΔU_{surf}. The SOC_{surf}–ΔU_{surf} relationship could actually be represented by the SOC–U_{OCV} curve with SOC_{surf} as the input, and Eq. (9) is hence rewritten as Eq. (10) while ΔU_{surf} is later represented by $U_{OCV}(SOC_{surf})$ as in Eq. (11). The SOC–U_{OCV} calibration is very common in present BMS development and the term SOC_{surf} could then be applied onboard without difficulty.

$$SOC_{surf,n} = \frac{c_{surf,n}}{c_{b,n}} \cdot SOC, \quad SOC_{surf,p} = \frac{c_{surf,p}}{c_{b,p}} \cdot SOC \tag{8}$$

$$U_t = \left(U_p\left(SOC_{surf,p}\right) - U_n\left(SOC_{surf,n}\right)\right) - U_0 - U_{DL,n} - U_{DL,p} \tag{9}$$

$$U_t = U_{OCV}\left(SOC_{surf}\right) - U_0 - U_{DL,n} - U_{DL,p} \tag{10}$$

$$\Delta U_{surf} = U_p\left(SOC_{surf,p}\right) - U_n\left(SOC_{surf,n}\right) = U_{OCV}\left(SOC_{surf}\right) \tag{11}$$

During battery operation, the macroscopic SOC is achievable by current integration method while the surface SOC could not be directly determined. As a result, the difference between SOC_{surf} and SOC (related to the difference of c_{surf} and c_b in solid-phase diffusion process following the Fick's second law) requires discussion to determine the terminal voltage. Considering the double layer effect [26], the current density $\bar{j}$ in the electrode is divided into the solid-phase-diffusional current density $\overline{j_{SD}}$ effective for the solid-phase diffusion and the double-layer current density $\overline{j_{DL}}$, and the three current densities ($\bar{j}$, $\overline{j_{SD}}$ and $\overline{j_{DL}}$) correspond separately to the macroscopic current I, solid-phase-diffusional current I_{SD} and double layer current I_{DL} as Eq. (12). The solid-phase-diffusional current I_{SD} is seen for simplicity as in one-state relationship with the current I with the time constant τ_{DL}, as in Eq. (13), and the voltage drop in the double layer (U_{DL}) is resulted from the resistance R_{CT} indicating the resistance effect of double layer in Eq. (14). In steady state under constant current input, the difference of c_{surf} and c_b (noted as $\Delta c_{stat,cc}$) is expressed in Eq. (15) [27], in which the concentration difference parameter $k_{SD,c}$ is defined with the unit $mol \cdot m^{-3} A^{-1}$. The particle radius R_s, active material volume fraction ε_s, electrode thickness δ, electrode plate area A, and solid-phase diffusion coefficient D_s are all constant for a specific battery under constant temperature, so $k_{SD,c}$ is seen as constant and $\Delta c_{stat,cc}$ is proportional to current input. The concentration difference Δc changes with time in dynamic current cases and is calculated by the finite difference method in Ref. [21], and the Δc variation under a current pulse was approximated as a first-order process for each electrode in Ref. [28], as in Eq. (16) with τ_{SD} the time constant. It is to be noted that the concentration difference Δc is related to a single electrode, and the difference between SOC and SOC_{surf} (ΔSOC) reflects the influence of both electrodes. The ΔSOC is hence determined by two first-order processes in Eq. (17), in which $k_{SD,1}$ and $k_{SD,2}$ are the SOC-difference parameters and $\tau_{SD,1}$ and $\tau_{SD,2}$ are the time constants.

$$\bar{j} = \bar{j}_{DL} + \bar{j}_{SD}, I = I_{DL} + I_{SD} \tag{12}$$

$$I_{SD} = I \cdot [1 - \exp(-t/\tau_{DL})] \tag{13}$$

$$U_{DL} = I_{SD} R_{CT} = I R_{CT} \cdot [1 - \exp(-t/\tau_{DL})] \tag{14}$$

$$\Delta c_{stat,cc} = c_b - c_{surf} = \frac{R_s^2 \bar{j}_{SD}}{15 D_s \varepsilon_s F} = \frac{R_s^2 I_{SD}}{15 D_s \varepsilon_s F A \delta} = k_{SD,c} I_{SD} \tag{15}$$

$$\Delta c = k_{SD,c} I_{SD} \cdot [1 - \exp(-t/\tau_{SD})] \tag{16}$$

$$\Delta SOC = k_{SD,1} I_{SD,1} \cdot [1 - \exp(-t/\tau_{SD,1})] + k_{SD,2} I_{SD,2} \cdot [1 - \exp(-t/\tau_{SD,2})] \tag{17}$$

2.2. Battery extended equivalent circuit model and model comparison

In this section, the voltage calculation process of the commonly-used battery models is evaluated according to the SPM-based analysis in Section 2.1, and the extended equivalent circuit model (EECM) is introduced with the enhanced estimation accuracy compared with the traditional ECM. The onboard-frequently-employed ECM consists of a pure resistor and several RC components, and the following discussion deals with the two-state ECM as shown in Fig. 2, in which the terminal voltage is expressed as Eqs. (18) and (19). Referencing the electrochemistry-based explanation in Eq. (6), the pure resistor R_o in the ECM reflects the instantaneous voltage drop U_0. The voltage source is looked up by the macroscopic SOC with the resulted $U_{OCV}(SOC)$ representing the open circuit voltage instead of the present potential $U_{OCV}(SOC_{surf})$, indicating that the difference between $U_{OCV}(SOC)$ and $U_{OCV}(SOC_{surf})$ referring to the solid-phase diffusion (noted as U_{SD} in Eq. (20)) needs specific consideration. The voltage drops owing to double layer effect ($U_{DL,n}$ and $U_{DL,p}$) could be determined by two one-state processes referring to Eq. (14) and hence included in the polarization voltages $U_{po,1}$ and $U_{po,2}$, noted as $U_{DL,n,ECM}$ and $U_{DL,p,ECM}$ respectively. As the only transient components in the ECM, the two RC components also reflect the solid-phase-diffusional voltage drop U_{SD} (the term reflected in the ECM noted as $U_{SD,ECM}$) to a certain extent, as in Eq. (21). In Eq. (22) for convenience, the polarization voltage terms ($U_{po,1}$ and $U_{po,2}$) are considered together as U_{po}, as well as the double-layer voltage drops $U_{DL,n,ECM}$ and $U_{DL,p,ECM}$ (considered together as $U_{DL,ECM}$).

$$U_t = U_{OCV}(SOC) - I \cdot R_o - U_{po,1} - U_{po,2} \tag{18}$$

$$U_{po,i} = I R_{po,i} \cdot [1 - \exp(-t/\tau_{po,i})], \quad i = 1,2 \tag{19}$$

$$U_{SD} = U_{OCV}(SOC) - U_{OCV}(SOC_{surf}) \tag{20}$$

$$U_{OCV,ECM}(SOC_{surf}) = U_{OCV}(SOC) + U_{SD,ECM} \tag{21}$$

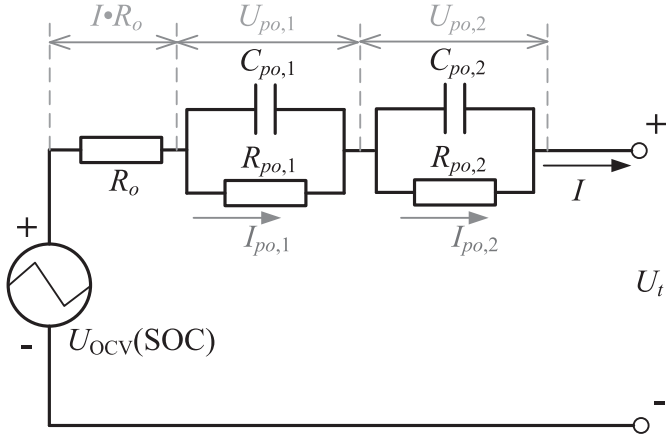

Fig. 2. Schematic of two-state battery equivalent circuit model (ECM).

$$U_{po} = U_{SD,ECM} + U_{DL,ECM} \tag{22}$$

Compared with the electrochemistry-based SPM discussed in Section 2.1 shown in Fig. 3(a), the ECM calculates the solid-phase-diffusional voltage change U_{SD} and double-layer-based voltage changes U_{DL} in a much simpler way, as illustrated in Fig. 3(b). For the simplified electrochemical process in Fig. 3(a), the solid-phase-diffusional current I_{SD} and the U_{DL} are in one-state relationship with the input current I according to Eqs. (13) and (14). The difference between SOC and SOC_{surf} (ΔSOC) related to the solid-phase diffusion is also one-state related to I_{SD}. To determine U_{SD}, the open circuit voltage $U_{OCV}(SOC)$ and the $U_{OCV}(SOC_{surf})$ are separately looked up by SOC and SOC_{surf} from the SOC–U_{OCV} relationship. Due to the strong nonlinearity of the SOC–U_{OCV} curve especially in low-SOC area, U_{SD} could not be proportionally related to ΔSOC. As a result, the solid-phase-diffusional U_{SD} is determined through a second-order process and a nonlinear mapping relation. In contrast, the solid-phase-diffusional voltage change $U_{SD,ECM}$ for the ECM is directly in one-state relationship with the macroscopic current as part of the polarization voltage U_{po}. As a result, the ECM-determined $U_{SD,ECM}$ may be inaccurate due to the following reasons. Firstly, the first-order process in ECM is used to simulate the second-order relationship in SPM, which lowers the voltage accuracy. Secondly, $U_{SD,ECM}$ and $U_{DL,ECM}$ are expressed together by U_{po}. Since the time constants of the double layer and the solid-phase diffusion processes are different, a compromise must be made to obtain the τ_{po}. And the $U_{SD,ECM}$ could not reflect the nonlinear relationship of U_{SD} and ΔSOC, which might be the key drawback of the traditional ECM.

In order to explain the necessity to consider the SOC–U_{OCV} nonlinearity, Fig. 4 discusses the determination of $U_{OCV}(SOC_{surf})$ under different current rates as an example. As a first order process in Eq. (19), the polarization voltage U_{po} at time point t is enlarged or reduced by a factor number a when the input current I is multiplied by a, i.e. $U_{po}(aI, t) = aU_{po}(I, t)$, and the ECM-based $U_{SD,ECM}$ is assumed to follow the same pattern $U_{SD,ECM}(aI, t) = aU_{SD,ECM}(I, t)$. The similar relationship is also for the second-order ΔSOC in SPM, i.e. $\Delta SOC(aI, t) = a\Delta SOC(I, t)$. In Fig. 4, the open circuit voltage is determined by the macroscopic SOC as $U_{OCV}(SOC)$, and the present ΔU_{surf} follows the SOC–U_{OCV} curve. At a certain time point t, the surface SOC under a relatively low current I_l is noted as $SOC_{surf,l}$, with the potential as $U_{OCV}(SOC_{surf,l})$. The difference between $SOC_{surf,l}$ and macroscopic SOC is ΔSOC_l. Assuming a perfect identification result for the ECM, in which the solid-phase-diffusional voltage

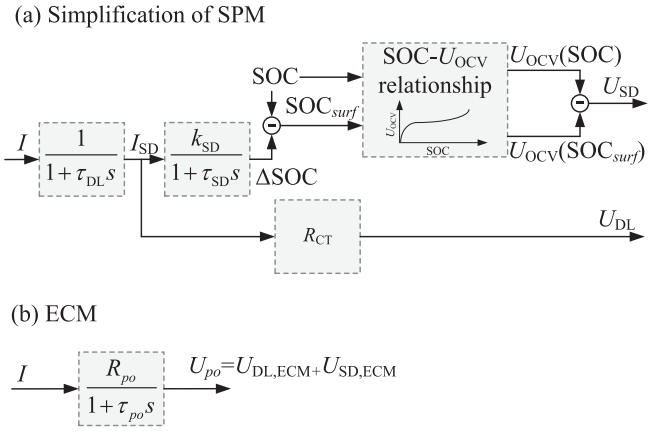

Fig. 3. Calculation of the solid-phase diffusional voltage change U_{SD} and the double-layer-based voltage changes U_{DL} based on different models: (a) based on simplified explanation of single-particle model; (b) based on equivalent circuit model.

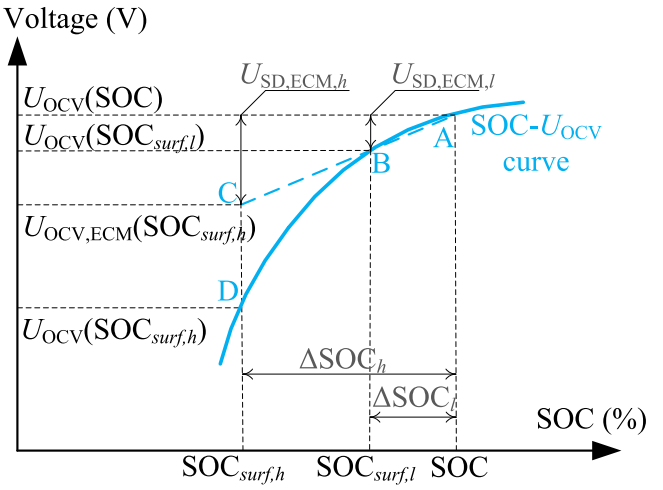

Fig. 4. Illustration of surface SOC and its influence on potential determination in the ECM.

drop $U_{SD,ECM,l}$ equals the subtraction of the open circuit voltage $U_{OCV}(SOC)$ and the $U_{OCV}(SOC_{surf,l})$. According to Eqs. (20) and (21), the ECM-estimated $U_{OCV,ECM}(SOC_{surf,l})$ equals $U_{OCV}(SOC_{surf,l})$. However, for another current rate I_h with $I_h = bI_l$ (b is the factor), the estimated result under I_l would lead to a certain error. From the above analysis, ΔSOC_h (the difference between $SOC_{surf,h}$ and macroscopic SOC) at time point t equals $b\Delta SOC_l$. For the ECM, the diffusional voltage drop $U_{SD,ECM,h}$ equals $bU_{SD,ECM,h}$. The ECM-estimated $U_{OCV,ECM}(SOC_{surf,h})$ could hence be determined geometrically as the intersection of the extrapolation of the blue-dashed AB and the y-direction line of $SOC_{surf,h}$, i.e. point C, which results in a large deviation from the real $U_{OCV}(SOC_{surf,h})$ (point D). For an arbitrary current input, the ECM-estimated value is on the extrapolation or interpolation of the AB line, meaning that the ECM could only provide linear approximation of the voltage drop in solid-phase diffusion. When the SOC–U_{OCV} curve shows good linearity, the ECM-determined value deviates not much from the real $U_{OCV}(SOC_{surf})$. When the SOC–U_{OCV} curve is very nonlinear (e.g. the case in Fig. 4), the gap between $U_{OCV,ECM}(SOC_{surf})$ and the real potential is very noteworthy.

For lithium-ion batteries, good linearity is generally shown for the SOC–U_{OCV} curve in high and middle SOC range, and consequently the ECM-determined voltage illustrates high accuracy. In low-SOC range, the open circuit voltage drops very rapidly and nonlinearly as SOC decreases, leading to a large voltage estimation error. For this reason, the ECM could not provide satisfactory estimation results in low-SOC cases. It is also the case for the impedance model with more complex structure. Although the description of the solid-phase diffusion is more accurate indicating preciser SOC_{surf} values, there is still no reflection of the SOC–U_{OCV} curve nonlinearity between the voltage drop $U_{SD,IM}$ and the ΔSOC. For the electrochemical models, e.g. the P2DM and the SPM, since the solid-phase diffusion process is specifically concerned and the cell potential is determined by the surface lithium concentration looking up the electrode potential relationship, the problem of linear approximation is avoided, and the low-SOC accuracy is also guaranteed [18]. But the electrochemical models depend on too many electrochemical parameters, which could hardly be determined or identified in real-world cases. And the high computational complexity also makes these models not applicable in onboard BMS chips.

The purpose of this paper is to present an accurate onboard-applicable battery model which represents the electrochemical process better than the traditional ECM. As discussed above, the ECM could reflect many of the electrochemical terms in Eq. (6) very well, including the instantaneous voltage change U_0 by the resistor R_o and the double-layer-based voltage changes ($U_{DL,n}$ and $U_{DL,p}$) by two RC components. But the U_{SD} arising from the solid-phase diffusion could only be linearly approximated in the ECM as in Fig. 4, which brings unignorable errors in the nonlinear period of the SOC–U_{OCV} relationship. As a result, this research seeks to introduce a component specifically reflecting the solid-phase diffusion instead of the RC elements used in the traditional ECM. The surface SOC is firstly estimated through the macroscopic SOC and the ΔSOC, and the present ΔU_{surf} is directly looked up as $U_{OCV}(SOC_{surf})$. The introduction of SOC_{surf} in the modified model avoids the linear approximation through the open circuit voltage $U_{OCV}(SOC)$ and the solid-phase-diffusion voltage drop U_{SD}, and in that case the shape of the nonlinear SOC–U_{OCV} curve could always be followed. According to Eq. (17), the term ΔSOC is achievable by two first-order processes, and could be expressed by two ΔSOC components (later noted as DSOC component). The modified model is named as the extended equivalent circuit model (EECM) with the schematic shown in Fig. 5. The EECM consists of a pure resistor, two RC elements, two DSOC components, and a voltage source. The RC components correspond respectively to the double-layer voltage change in negative and positive electrode (noted as $U_{DL,1}$ and $U_{DL,2}$, as in Eq. (23)), with the solid-phase-diffusional current $I_{SD,1}$ and $I_{SD,2}$ calculated in Eq. (24). The DSOC components are also one-state but with the solid-phase-diffusional current terms as input and SOC offset as output in Eq. (25). The output ΔSOC_1 and ΔSOC_2 is then combined with the macroscopic SOC to determine the SOC_{surf} in Eq. (26), which is then employed by the voltage source to obtain the $U_{OCV}(SOC_{surf})$ directly. Consequently, the terminal voltage of EECM is determined as in Eq. (27). Referencing the electrochemical terms in Eq. (6), Table 2 compares the EECM and the traditional ECM.

$$U_{DL,i} = IR_{CT,i}\cdot\left[1-\exp\left(-t/\tau_{DL,i}\right)\right],\quad i=1,2 \tag{23}$$

$$I_{SD,i} = U_{DL,i}/R_{CT,i},\quad i=1,2 \tag{24}$$

$$\Delta SOC_i = k_{SD,i}I_{SD,i}\cdot\left[1-\exp\left(-t/\tau_{SD,i}\right)\right],\quad i=1,2 \tag{25}$$

$$SOC_{surf} = SOC - \Delta SOC_1 - \Delta SOC_2 \tag{26}$$

$$U_t = U_{OCV}\left(SOC_{surf}\right) - I\cdot R_o - U_{DL,1} - U_{DL,2} \tag{27}$$

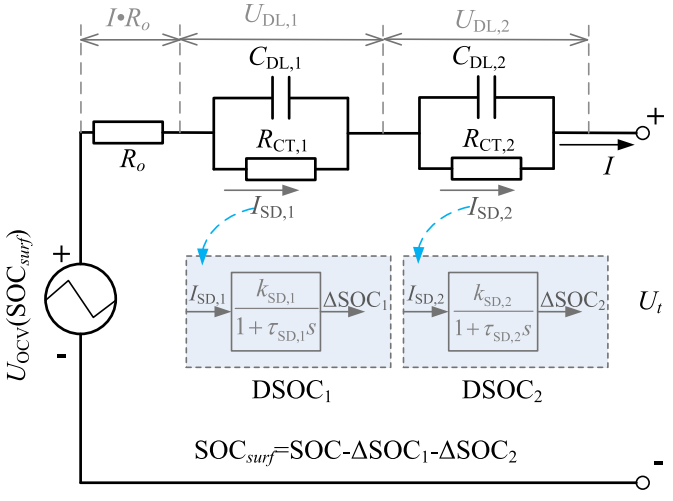

Fig. 5. Schematic of battery extended equivalent circuit model (EECM).

Table 2
Comparison of ECM and EECM in terminal voltage determination.

Electrochemical terms	Related terms in ECM	Related terms in EECM
Instantaneous voltage change (U_0)	Resistor R_o	Resistor R_o
Double-layer-based voltage change (U_{DL})	RC components	RC components
Solid-phase-diffusional voltage change (U_{SD})	RC components (linear approximation)	DSOC components
Voltage source output (U_{OCV})	Macroscopic SOC	Surface SOC (SOC_{surf})

Compared with the traditional ECM, only two one-state DSOC elements are added in the EECM, resulting in relatively limited increase in model complexity and a promising implementation in real-world BMS applications. The introduction of SOC_{surf} indicates the direct determination of ΔU_{surf} in dynamic operations and the model could hence reflect the nonlinearity of potential variation. In that case, an evident improvement in low-SOC-area performance could be made by the EECM in contrast to the ECM.

3. Experimental and model parameter identification

3.1. Experimental setup

In this research, a type of commercial prismatic lithium nickel–cobalt–manganese oxide/graphite (NCM-G) battery with 20-Ah nominal capacity was tested, in which the NCM-G system acts as a good candidate in the PEV application for its high specific energy and good cycle life performance [29]. The basic battery parameters are listed in Table 3. Note that the C-rate is related to the nominal capacity Q_{nom} (20 Ah), and the SOC value is calculated according to the standard capacity Q_{st}. The charge and discharge process was executed on a Neware BTS-3000 test bench with current range −100 to 100 A. A DGBELL BE-HL-150M3 temperature chamber (temperature range −40 to 150 °C, temperature error within ±0.3 °C) was used to limit the temperature fluctuation. The chamber was set at 25 °C in this research, and the actual temperature variation in all the experiments was very limited (within 24.8 °C and 26.2 °C), indicating the temperature influence on battery parameters as negligible. For real-world applications with large temperature range, a parameter calibration process under different temperatures as well as an electro-thermal model is needed, which is beyond the main scope of this work and will be discussed in the future.

Table 3
Basic parameters of test battery according to product specifications.

Parameter	Value
Material	$Li(Ni_xMn_yCo_{1-x-y})O_2$/graphite
Nominal capacity (Ah)	20
Maximum continuous discharge current (A)	4 C (80 A)
Maximum continuous charge current (A)	1 C (20 A)
Allowed voltage range (V)	2.75 to 4.2
Allowed temperature range for discharge (°C)	−20 to 55
Allowed temperature range for charge (°C)	0 to 45
Recommended charging method	Constant current charge (0.5 C, 10 A), then constant voltage charge until 0.05 C (1 A)

The model parameterization is based on a set of experiments modified from the hybrid pulse power characterization (HPPC) test [30]. The original HPPC test with 10 s discharge, 40 s pause and 10 s charge was designed for the hybrid electric vehicle application, and the pulse profile is modified here by lengthening the discharge period to 30 s to fit the PEV case, as the current profile shown in Fig. 6 with discharge current 40 A (2 C) and charge current 30 A (1.5 C). The constant-current discharge period (0.5 C discharge for 280 s, for a total of 5% SOC change in one current profile) after the charge pulse is also included to guarantee the resulted parameters suitable for the profiles with large current variation as well as those with stable current. With a 5% SOC gap, the test profile was executed 21 times from 100% to 0% SOC to examine the SOC influence on parameter identification results, and implemented on two cells (namely cell 1 and cell 2) to check the model performance considering cell inconsistency. The standard capacity Q_{st} is approximately 20.8 Ah for cell 1 and 20.6 Ah for cell 2 during our test.

In order to obtain a detailed SOC–U_{OCV} relationship for the EECM rather than interpolating the limited HPPC test points, the battery was discharged and charged under 0.02 C (0.4 A), and the averaged voltage from the low-rate discharging and charging process is treated as the SOC–U_{OCV} curve, as shown in Fig. 7, which coincides well with the HPPC-resulted points. It is noted that the curve in high and middle SOC range is relatively linear and the period under 15% SOC shows obvious nonlinearity and large slope. This curve is later implemented in the EECM and the ECM, in which the EECM uses surface SOC to look up the potential while the traditional ECM uses SOC instead.

The model estimation accuracy is validated depending on the experiments under the constant-current discharge pause profile (DPP) and the dynamic stress test (DST) profile, which would be described detailedly in Section 4.

3.2. Parameter identification and results comparison

In this section, the measured voltage response under HPPC profile is employed to identify the parameters of the EECM under different SOCs, and the parameterization process is executed on the traditional ECM (with the two-state equivalent circuit model as a representative) for comparison. There exist a large number of parameters to be identified (six parameters for ECM and ten for EECM, listed in Tables 4 and 5), and a robust and intelligent identification

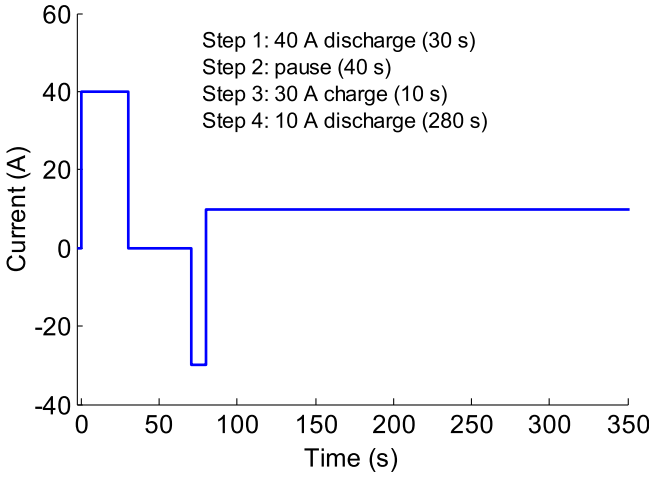

Fig. 6. Current profile for parameter identification of ECM and EECM.

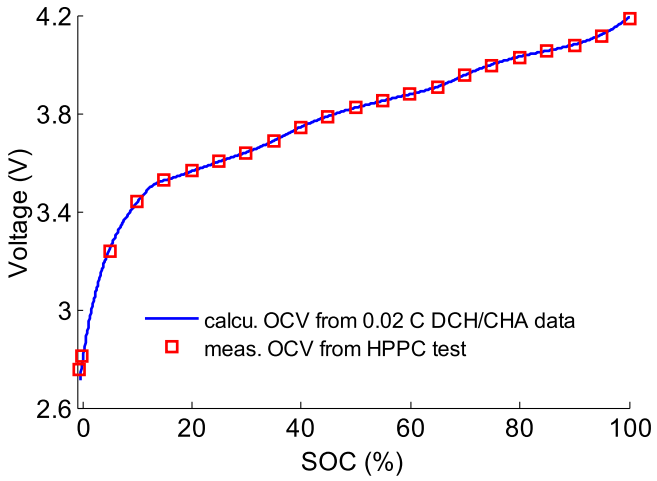

Fig. 7. Comparison of calculated SOC–U_{OCV} relationship through 0.02 C discharge/charge data and measured SOC–U_{OCV} from HPPC test.

method is needed to obtain the optimum results. Therefore, the genetic algorithm (GA) developed by Holland [31] is a proper choice. The GA is a global optimization method which could find the optimum for complex objective functions effectively and is hence employed here for the model parameterization. The model voltage output follows Eq. (27) for EECM and Eq. (18) for ECM, and the GA is applied to determine the optimum parameters by minimizing the root mean square error between voltage measurement and model-calculated voltage.

The to-be-identified parameters of ECM and EECM are listed in Tables 4 and 5 referencing Figs. 2 and 5. The ohmic resistance values in discharging and charging process are separately determined and noted as $R_{o,d}$ and $R_{o,c}$, and the upper and lower bounds of the parameters in GA calculation are empirically decided.

The parameterization is based on the experimental data of cell 1, and the accuracy of the obtained model is examined by the data of cell 1 as well as cell 2. The parameterization data source and the validation profile are identical for the cell 1 case, which is actually the fidelity examination of the identification process. The root mean square errors (RMSEs) of the model-calculated at different SOCs are shown in Fig. 8 as blue markers (in the web version) for ECM and red markers for EECM. Both models demonstrate good accuracy at SOCs larger than 20%, in which the average RMSE resulted from ECM is about 2 mV, while the case for the EECM is approximately 1 mV. In the lower-than-20% SOC range, the difference between the two models becomes more obvious and the EECM shows evidently better accuracy. For instance, the error of EECM at 5% SOC is lower than 10 mV while in contrast the ECM-based RMSE exceeds 30 mV. It is therefore illustrated that the EECM occupies a much better performance than the ECM in low-SOC area.

The model-calculated voltage is compared with the measurement result in Fig. 9. The results at two SOC points representing the middle-SOC area (50% SOC, in Fig. 9a) and the low-SOC area (5% SOC, in Fig. 9b) are shown to compare the fitting results of the ECM and the EECM. At 50% SOC, the voltage results from both models follow the experimental data tightly, while at 5% SOC the EECM-determined voltage traces the nonlinear variation of the measurement very well to bring a much smaller error than the traditional ECM. It is consequently expressed that the EECM with SOC_{surf} determination has a certain advantage over the ECM in case of nonlinear battery properties at low SOCs.

It is essential to check the performance of identified model parameters on different cells in consideration of the cell inconsistency [32]. The model parameters identified from cell 1 are employed on the profile in cell 2, and the resulted RMSEs are shown in Fig. 10. It is noticed that the RMSE values increases a little bit compared with Fig. 8 due to cell variance, while the errors at relatively large SOC are still very limited (3 mV for ECM and 2 mV for EECM). When the SOC is under 20%, high benefits could also be made by the EECM to reduce voltage error.

Fig. 11 compares the model-determined voltage output and the measured voltage on cell 2, with Fig. 11a at 50% SOC and Fig. 11b at 5% SOC. The estimation results are satisfying for both models at 50% SOC with only slightly RMSE increase, and the EECM could still guarantee its extraordinary accuracy at low SOC on a different cell. As a result, the EECM is applicable for the battery pack with cell differences to enhance the low-SOC-area estimation performance.

Table 4
Parameters to be identified in ECM.

Parameter	Description	Unit
$R_{o,d}$	Discharging ohmic resistance	Ω
$R_{o,c}$	Charging ohmic resistance	Ω
$R_{po,1}$	Resistance of the first polarization process	Ω
$\tau_{po,1}$	Time constant of the first polarization process	s
$R_{po,2}$	Resistance of the second polarization process	Ω
$\tau_{po,2}$	Time constant of the second polarization process	s

Table 5
Parameters to be identified in EECM.

Parameter	Description	Unit
$R_{o,d}$	Discharging ohmic resistance	Ω
$R_{o,c}$	Charging ohmic resistance	Ω
$R_{CT,1}$	Resistance of the first double-layer process	Ω
$\tau_{DL,1}$	Time constant of the first double-layer process	s
$R_{CT,2}$	Resistance of the second double-layer process	Ω
$\tau_{DL,2}$	Time constant of the second double-layer process	s
$k_{SD,1}$	SOC-difference parameter of the first ΔSOC process	–
$\tau_{SD,1}$	Time constant of the first ΔSOC process	s
$k_{SD,2}$	SOC-difference parameter of the second ΔSOC process	–
$\tau_{SD,2}$	Time constant of the second ΔSOC process	s

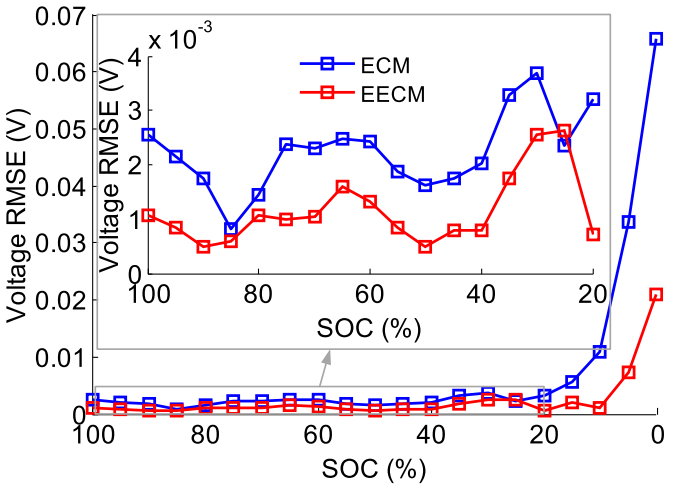

Fig. 8. Voltage RMSE comparison of ECM and EECM under the parameterization profile at different SOCs on the same cell (cell 1).

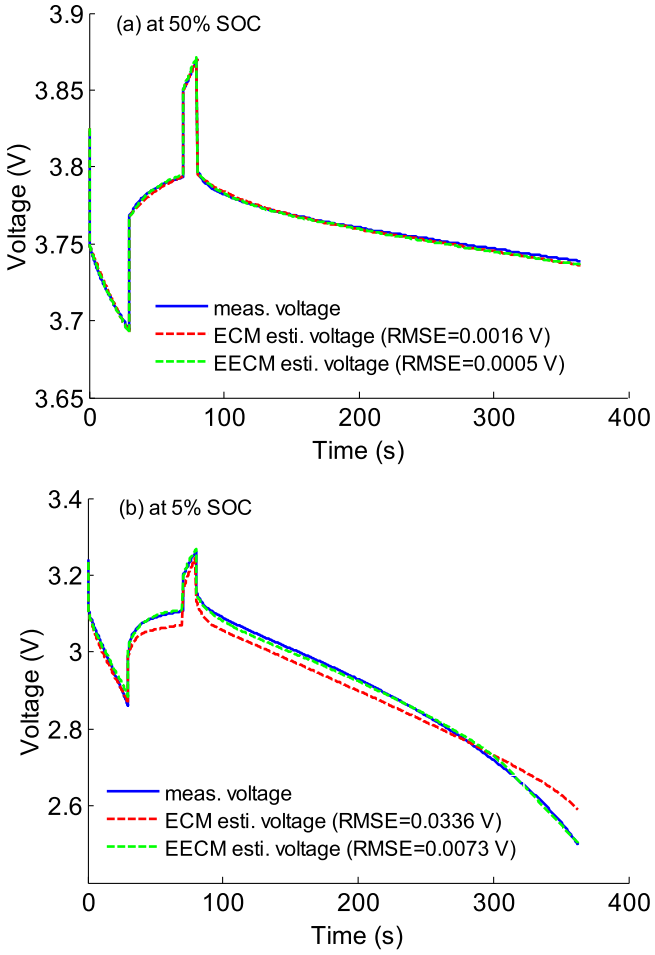

Fig. 9. Voltage estimation results of ECM and EECM under the parameterization profile on the same cell (cell 1): (a) at 50% SOC; (b) at 5% SOC.

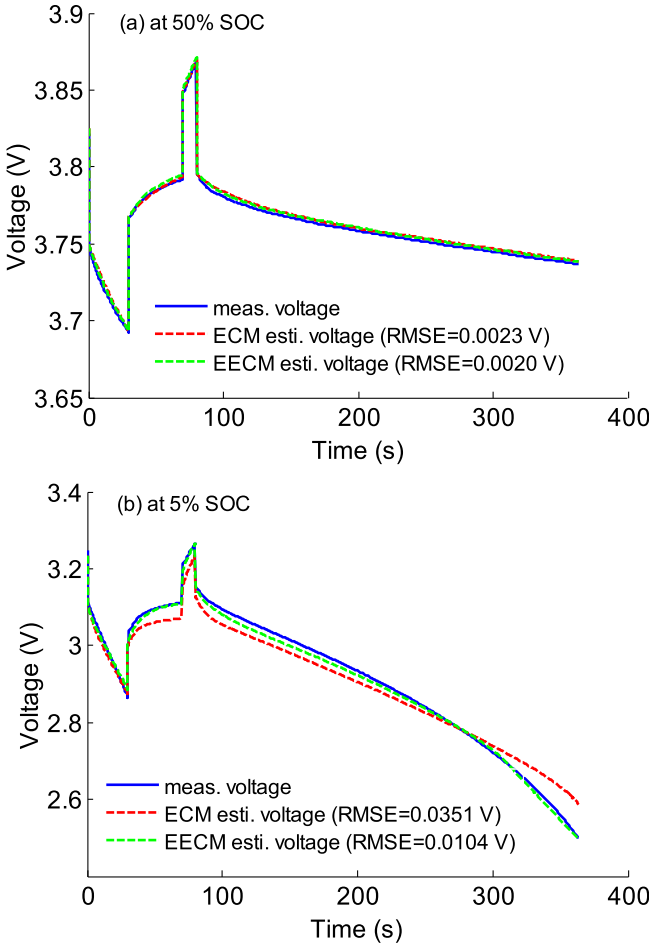

Fig. 11. Voltage estimation results of ECM and EECM under the parameterization profile on a different cell (cell 2): (a) at 50% SOC; (b) at 5% SOC.

4. Model verification under different load profiles

In this section, the voltage estimation accuracy of the EECM is verified under different load profiles based on the identified parameters in Section 3. To validate the model effectiveness and the advantage over the original ECM, two load profiles are implemented in the verification process, namely the constant-current discharge pause profile (DPP) in Section 4.1 and the dynamic stress test (DST) profile in Section 4.2. It is to be noticed that the model input is the current or power profile in the whole test period indicating an offline computing process, which is different from the online SOC estimation case in Section 5 with real-time voltage update.

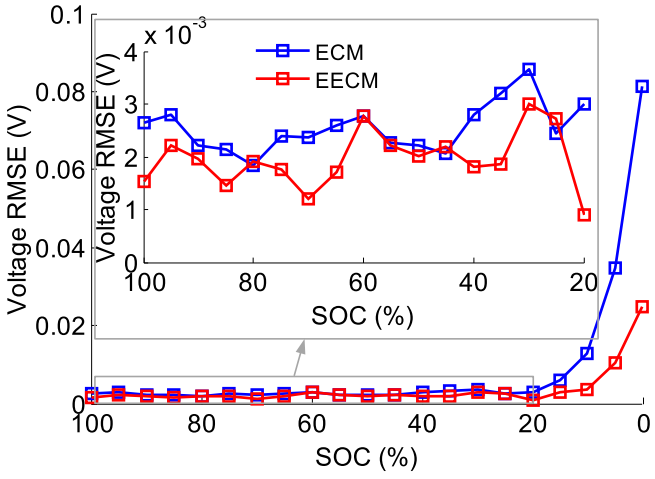

Fig. 10. Voltage RMSE comparison of ECM and EECM under the parameterization profile at different SOCs on a different cell (cell 2).

4.1. Results under constant-current discharge pause profile

The performance of EECM is firstly evaluated under a set of constant-current discharge pause profiles (DPP). The DPP is determined as a two-period cycle, in which the battery experiences constant-current discharge in the first period and rests in the second period, and cycles from the fully charged state until the discharge voltage limit. The long constant-current discharge period aims to simulate the stable driving condition with relatively constant speed and power demand, and the rest period is to check the voltage estimation accuracy in the depolarization process. Three groups of DPP tests were carried out with the current values 10 A (0.5 C), 20 A (1 C), and 40 A (2 C) respectively, in which the lengths of the discharge periods were respectively 20 min, 10 min, and 5 min to get an identical discharge coulomb amount and hence an identical SOC change for each DPP cycle, in order to examine the influence of discharge rate on model accuracy in the same SOC area.

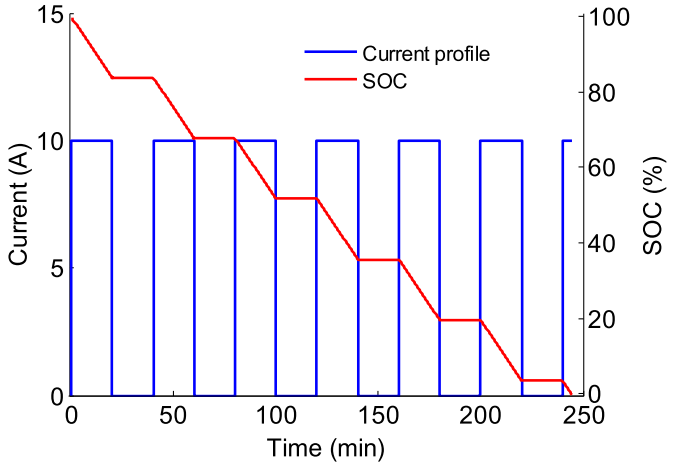

Fig. 12. Current and SOC variation of discharge-pause profile (under 0.5 C DPP).

Each test was with a uniform 20-min rest time. The current profile and the corresponded SOC variation are illustrated in Fig. 12 with the 0.5C DPP as an example, in which six complete DPP cycles are accomplished and the battery reaches the discharge limit in the seventh discharge period. It is to be noted that the validation experiments in Section 4.1 and 4.2 were carried out on cell 2 (with the model parameters identified on cell 1) to check the model applicability considering cell inconsistency.

Under 0.5 C DPP test, the estimated voltages of the ECM and EECM are compared with the measured voltage in Fig. 13a, with the voltage error shown in Fig. 14a. Note that the error is determined by the measured value subtracted by the estimated value, so that a positive error indicates that the model underestimates the voltage while a negative error implies overestimation. The green dashed lines (in the web version) in Fig. 14 reflect the 10 mV and −10 mV error boundaries. It is shown in Figs. 13a and 14a that both the ECM and the EECM provide accurate results at the beginning and middle periods of the test with the errors within ±10 mV. Starting from the sixth cycle with SOC lower than 19.5%, the estimated voltages show larger deviation from the real value, but the EECM could still guarantee a low voltage error (lower than 20 mV) in contrast to the ECM with maximum 60 mV underestimation. It is also noticed that the voltage accuracy in the rest period is improved by the EECM, which could hence be implemented in the adaptive estimation method of open circuit voltage [33]. The voltage comparison and the estimation errors under 1 C DPP test are demonstrated in Figs. 13b and 14b, and similarly the low-SOC-range voltage error of the EECM is much lower than that of ECM (max. 30 mV versus max. 100 mV). The analysis of the 2 C DPP case in Figs. 13c and 14c also leads to the same conclusion that the EECM significantly reduces the low-SOC-area voltage error (max. 50 mV versus max. 130 mV). By comparing the voltage error under different discharge currents in Fig. 14a, b and c, it is clear that the model estimation error increases at the current grows, and the EECM could limit the voltage error in a much smaller range than the ECM and consequently upgrade the low-SOC-area accuracy under different discharge currents.

The RMSE values under different SOC ranges and currents are then compared, in which the voltage RMSE is calculated by the mean voltage error in the discharge period of each DPP cycle. Fig. 15 lists the RMSE values of EECM and ECM related to SOC, and the SOC value is treated as the mean SOC of each complete discharge period, i.e. 92.0%, 75.9%, 59.8%, 43.7%, 27.6%, and 11.5% respectively. The blue markers are for the ECM and the red for EECM, while the square, circle, and triangle markers indicate separately the errors in

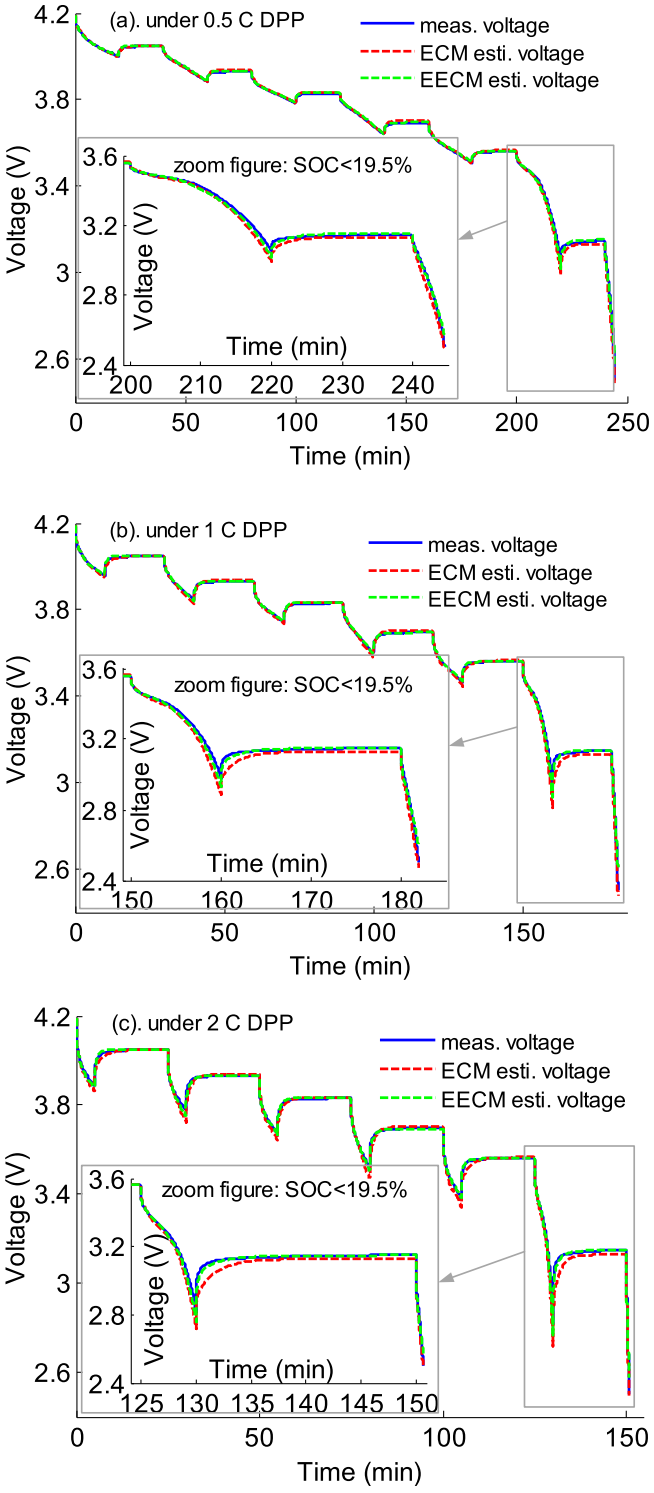

Fig. 13. Voltage estimation results of ECM and EECM in DPP test with different current values: (a) under 0.5 C DPP; (b) under 1 C DPP; (c) under 2 C DPP.

0.5 C, 1 C, and 2 C DPP cases. At SOC larger than 20%, the RMSE values are relatively independent from the SOC variation for both models. The lower-than-20% SOC leads to a large RMSE increase, while the EECM-based RMSE values are reduced by more than 50% compared with the ECM (e.g. 19 mV versus 41 mV in 2 C DPP case). Additionally, the ECM-based RMSE result grows rapidly when the current increases, while the EECM-based error is well controlled

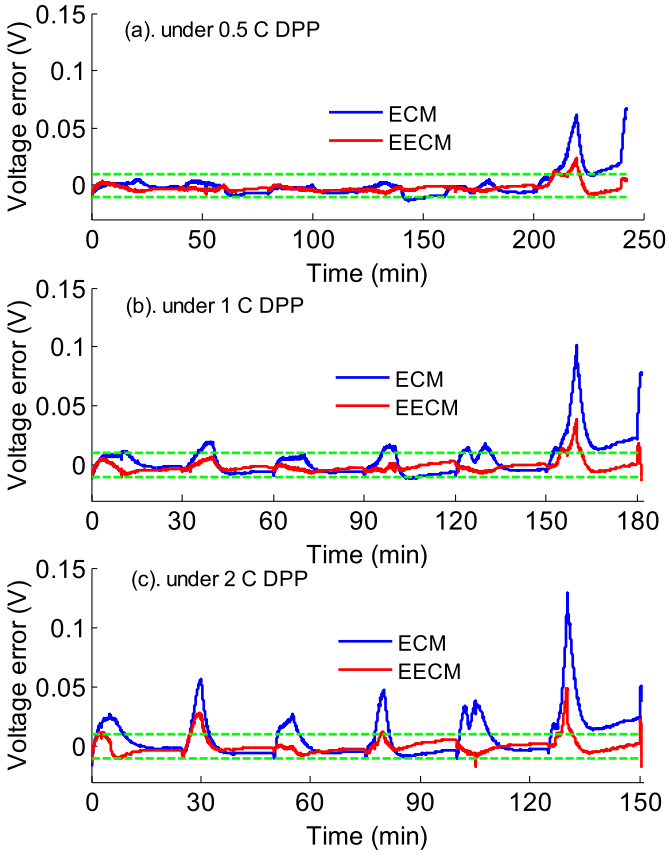

Fig. 14. Voltage error comparison of ECM and EECM in DPP test: (a) under 0.5 C DPP; (b) under 1 C DPP; (c) under 2 C DPP.

under different current rates, with the error lower than 10 mV at high SOC and under 20 mV in low-SOC range.

Different from the traditional ECM, the EECM determines the cell potential as well as the resistance parameters through the surface SOC rather than the macroscopic SOC, from which a better reflection of the nonlinearity in voltage variation is resulted. As in Eq. (26), the SOC_{surf} must be determined before the terminal voltage calculation. Taking the 2 C DPP test as an example, the variation of the macroscopic SOC and the SOC_{surf} is shown in Fig. 16,

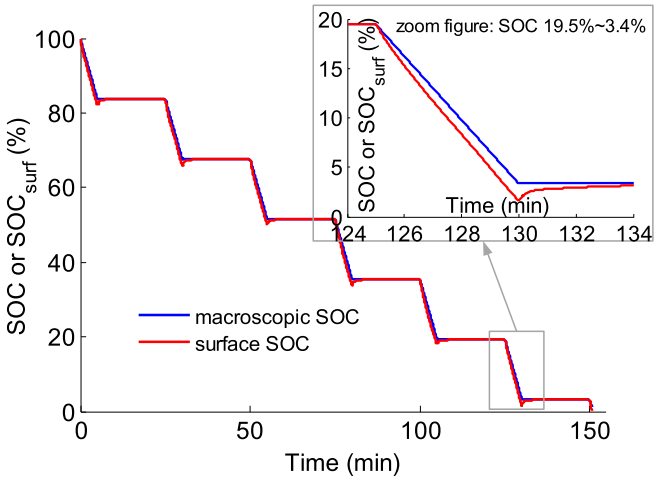

Fig. 16. Variation of SOC and surface SOC (SOC_{surf}) under 2 C DPP.

and the SOC_{surf} is always smaller than the average SOC due to a non-negative discharge current. From the zoom figure of the last discharge period, it is illustrated that the gap between SOC and SOC_{surf} increases during discharge owing to the progress of solid-phase diffusion, and the rest minutes diminish the SOC−SOC_{surf} gap indicating the balancing process of the surface-bulk concentration difference in the electrode particle.

Under different current rates, the SOC−SOC_{surf} gap in relation to SOC is shown in Fig. 17. As expressed in Fig. 4, the SOC−SOC_{surf} deviation (ΔSOC) endows the EECM with nonlinear capability in ΔU_{surf} determination instead of the linear voltage approximation from the macroscopic SOC point, which results in the advantage over the ECM in voltage estimation performance. Under larger discharge current, the ΔSOC is larger for the EECM and could consequently represent the voltage nonlinearity more evidently, and the model benefit over the ECM is for that reason larger, which is in accordance with the RMSE results in Fig. 15. The ΔSOC tends to increase as the discharge continues, and the ΔSOC-variation is probably caused by the variation of the identified DSOC-related parameters ($k_{SD,1}$, $\tau_{SD,1}$, $k_{SD,2}$, and $\tau_{SD,2}$) considering SOC change. To sum up, the performance of the EECM is validated under DPP tests with different rates, and the advantage over the

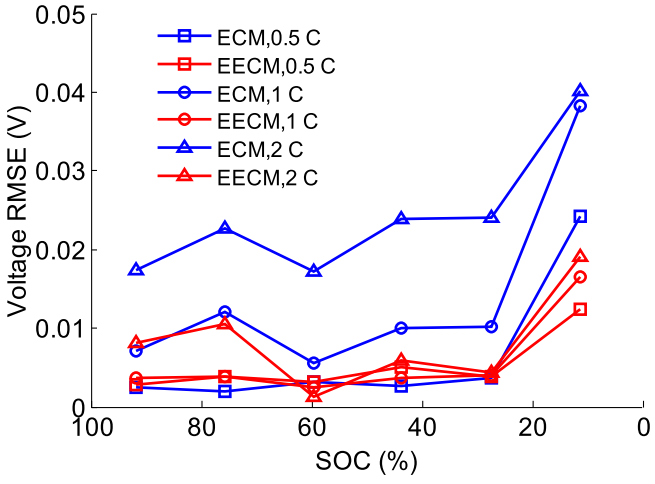

Fig. 15. Voltage RMSE comparison of ECM and EECM in DPP test at different SOCs.

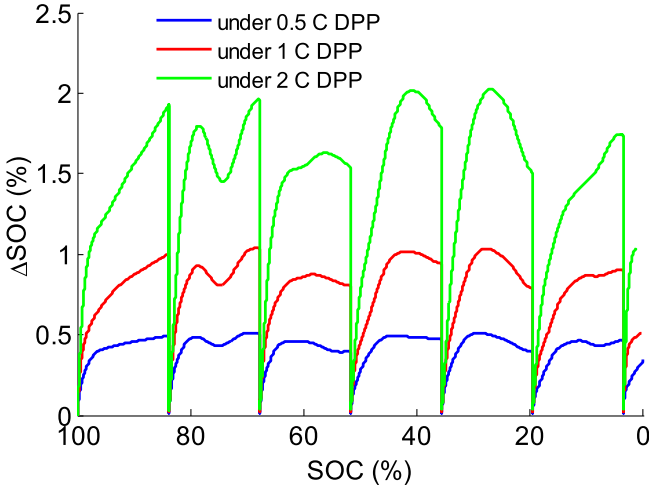

Fig. 17. Variation of the SOC−SOC_{surf} deviation (ΔSOC) in relation to SOC in DPP test.

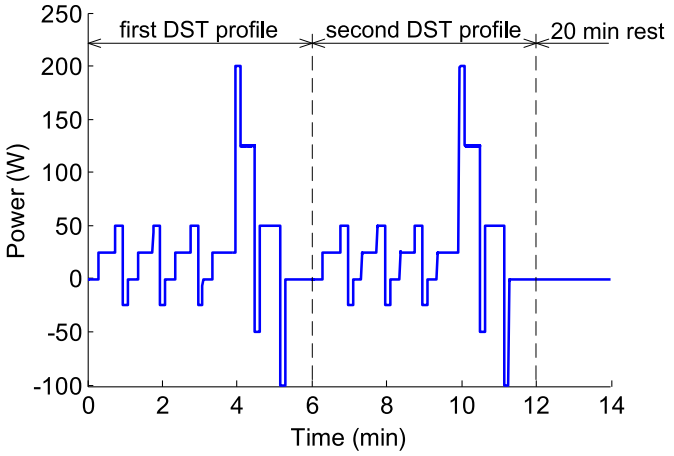

Fig. 18. Power profile of DST test cycle.

ECM is shown in voltage estimation accuracy especially in low-SOC cases.

4.2. Results under DST profile

The model validation is then carried out under the dynamic stress test (DST) load profile. The DST profile is a typical dynamic experiment cycle to test the battery dynamic properties reflecting the power demand in dynamic EV driving conditions [34]. The DST is here realized as a determined power profile, with the largest discharge power 200 W to keep the current under the maximum allowable discharge current 80 A. As shown in Fig. 18, an experiment cycle is determined here as two consecutive DSTs followed by a 20-min rest period. To prevent overcharging at the fully-charged battery state, the test is performed starting from 70% SOC until the end of discharge.

The estimated voltages of the ECM and EECM are compared with the measured voltage under DST profile in Fig. 19. A total of ten complete DST cycles are accomplished, and the 4th and 10th cycles are analyzed in detail. Fig. 20a corresponds to the voltage results in the 4th cycle with SOC 50.7%–43.9% representing the middle-SOC range and Fig. 21a illustrates the voltage error with the green dashed lines (in the web version) as the ±10 mV boundaries. Both the ECM and the EECM provide accurate results with the errors

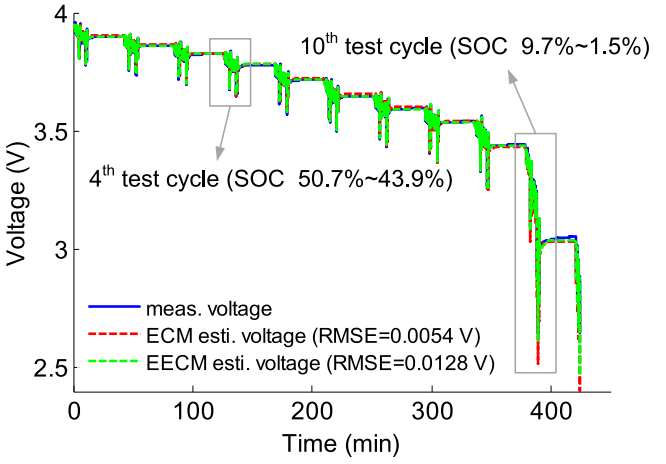

Fig. 19. Voltage estimation results of ECM and EECM under DST profile.

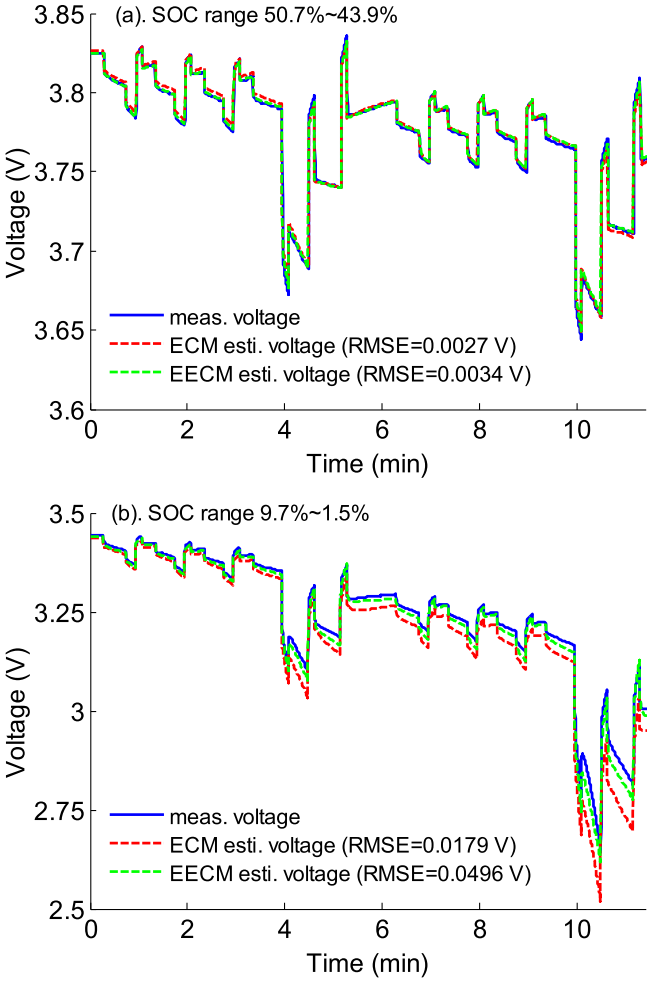

Fig. 20. Voltage estimation results of ECM and EECM in DST test cycles with different SOC ranges: (a) 4th test cycle with SOC range 50.7%–43.9%; (b) 10th test cycle with SOC range 9.7%–1.5%.

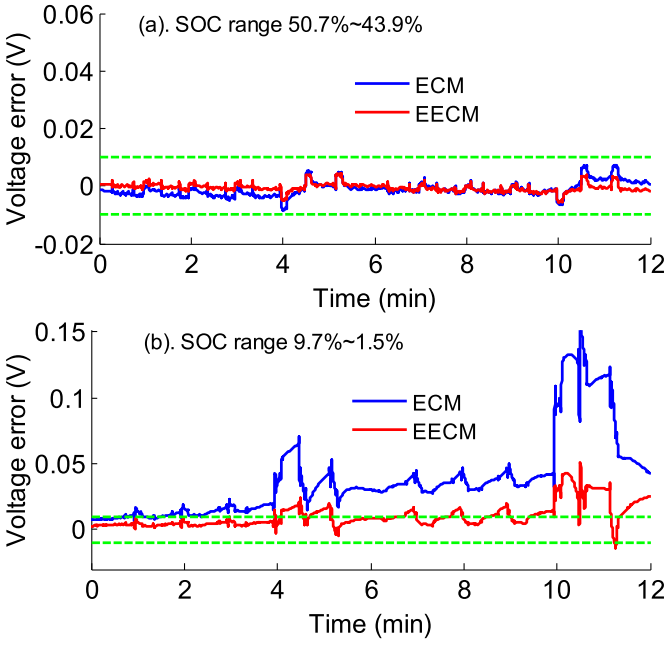

Fig. 21. Voltage error comparison of ECM and EECM in DST test cycles with different SOC ranges: (a) 4th test cycle with SOC range 50.7%–43.9%; (b) 10th test cycle with SOC range 9.7%–1.5%.

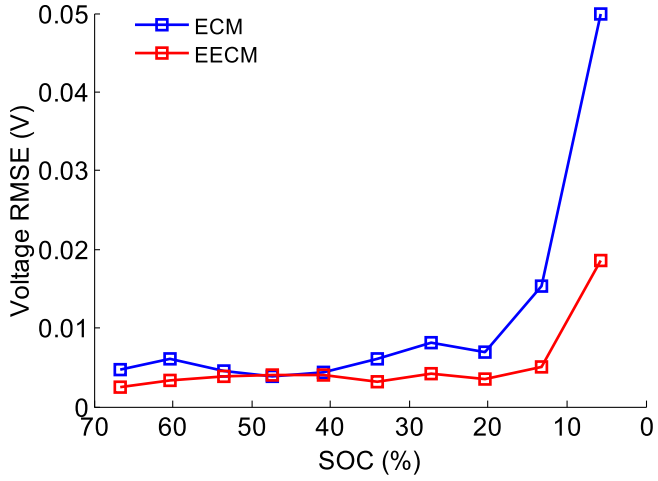

Fig. 22. Voltage RMSE comparison of ECM and EECM under DST profile at different SOCs.

within ±10 mV and fulfill the normal onboard accuracy requirement [35] while the EECM-based error is slightly smaller. Figs. 20b and 21b are related to the 10th cycle in low-SOC area with SOC 9.7%–1.5%, and the EECM presents obviously better voltage simulation results with the RMSE decreased by 64% (17.9 mV versus 49.6 mV) and the maximum error decreased by 66% (52 mV versus 151 mV). As a result, the low-SOC-range voltage error under dynamic load conditions could be significantly reduced with the implementation of the EECM.

The RMSE values under different SOC ranges are then compared in Fig. 22 with the voltage RMSE calculated by the mean error in two consecutive DSTs of each cycle, in which the SOC value is treated as the mean SOCs of each consecutive DST period, i.e. 66.6%, 60.3%, 53.7%, 47.4%, 40.8%, 34.1%, 27.3%, 20.4%, 13.3%, and 5.8% respectively. At SOC larger than 20%, the RMSE values are relatively stable and both the ECM-based and EECM-based errors are kept under 10 mV. For the ECM, the RMSE increases largely at SOC lower than 20%, especially in the lower-than-10% SOC area, while the EECM-based error is well controlled under 20 mV. It is verified that although the EECM could only slightly increase the voltage accuracy in high-SOC area, the effectiveness of the extended ECM is explicit for the error reduction in low-SOC cases.

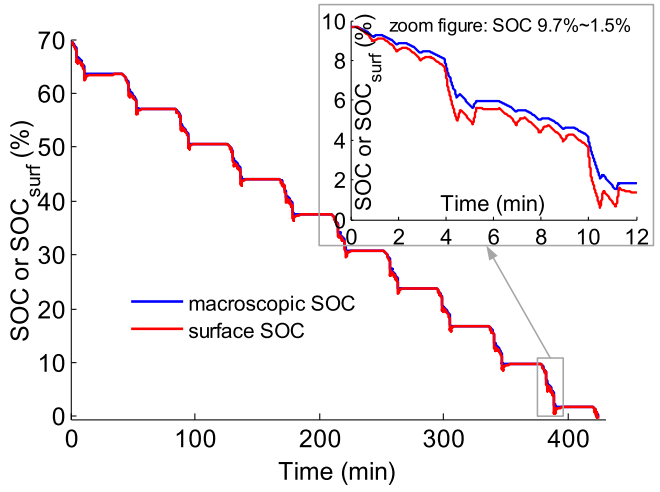

Fig. 23. Variation of SOC and surface SOC (SOC_{surf}) in EECM under DST load.

Fig. 23 shows the variation of the macroscopic SOC and SOC_{surf} in the EECM under DST profile. From the zoom figure of the last test period, it is known that the gap between SOC and SOC_{surf} (i.e. ΔSOC) varies frequently due to the dynamic discharging and charging loads in DST. In the high-power discharge periods with maximum current 72 A (3.6 C), the ΔSOC increases rapidly and reaches an apex of 1.5%, which makes the voltage nonlinearity more obviously and results in a larger advantage over ECM, as reflected by the error curves in Fig. 21b.

5. SOC estimation results based on the extended equivalent circuit model

5.1. SOC estimation system based on the EECM through extended Kalman filtering

In the vehicle onboard battery management system, the battery model is the basis of state estimation, which includes the voltage model, the aging model, the temperature model, and the safety model, etc. to determine the battery remaining discharge energy (E_{RDE}), the power capability, the remaining useful life, and the safety state [36–38]. The battery voltage model discussed in this paper is mainly employed to estimate the state of charge (SOC) real-timely, which is further used for the remaining discharge energy (E_{RDE}) and remaining driving range (RDR) determination. There exist a large number of model-based methods for online SOC estimation [13,36,39–41], in which a series of adaptive algorithms (i.e. Kalman filtering, extended Kalman filtering, sigma-point Kalman filtering, particle filtering, H-infinity, etc.) attract high attention. These methods combine the coulomb counting results and the model voltage outputs to obtain good accuracy. The extended Kalman filtering (EKF) is applicable for nonlinear system and the computational process is relatively simple compared with most other adaptive methods, so that it can be executed very accurately and continuously in onboard controllers. There exists a considerable influence on EKF performance from the accuracy of the employed model, and the model accuracy could hence be evaluated through the SOC estimation results based on different models. As a result, the EKF estimator is respectively carried out based on ECM and EECM to obtain the SOC estimation outcomes.

The battery model needs to be converted into a discrete state-space form in real-time applications. At the present time point t_k, the state equation and the measurement equation of the battery system are expressed in Eqs. (28) and (29), in which x_k is the system state vector. The terms u_k and y_k represent respectively the current input and output which stand here for the measured current I and terminal voltage U_t, while the process noise and the measurement noise are written as w_k and v_k. $f(x_{k-1}, u_k)$ is the nonlinear state transition function and $g(x_k, u_k)$ is the nonlinear measurement function. In EKF, both $f(x_{k-1}, u_k)$ and $g(x_k, u_k)$ are linearized in each time step by first-order Taylor expansion and hence expressed as the parameter matrices A_k, B_k, C_k, and D_k, as in Eq. (30). Since the battery parameters are affected by state factors such as SOC and temperature, the parameters in the matrices need to be looked up during operation, indicating a linear-parameter-varying (LPV) system. The coulomb-counting information combined in the EKF estimator is shown in Eq. (31), which is used to determine the prior state estimate $\hat{x}_k^-$ in a new time step. u_k is the current input at time k, Δt is the sample time, Q_{st} is the battery standard capacity, and η is the coulomb efficiency which is determined as 1 for the later calculation.

$$x_k = f(x_{k-1}, u_k) + w_k \tag{28}$$

$$y_k = g(x_k, u_k) + v_k \tag{29}$$

$$\begin{cases} A_k = \dfrac{\partial f(x_{k-1}, u_k)}{\partial x_{k-1}}\Big|_{x=\,\widehat{x}_{k-1}^{+}}, B_k = \dfrac{\partial f(x_{k-1}, u_k)}{\partial u_k}\Big|_{x=\,\widehat{x}_{k-1}^{+}} \\ C_k = \dfrac{\partial g(x_k, u_k)}{\partial x_k}\Big|_{x=\,\widehat{x}_k^{-}}, D_k = \dfrac{\partial g(x_k, u_k)}{\partial u_k}\Big|_{x=\,\widehat{x}_k^{-}} \end{cases} \tag{30}$$

$$\mathrm{SOC}_k = \mathrm{SOC}_{k-1} - u_k \cdot \frac{\Delta t}{Q_{\mathrm{st}} \cdot \eta \cdot 3600} \tag{31}$$

The SOC estimator based on the two-state ECM is firstly expressed with the state vector $x_{\mathrm{ECM},k}$ in Eq. (32), in which SOC_k, $U_{\mathrm{po},1,k}$, and $U_{\mathrm{po},2,k}$ are the SOC value and the polarization voltages on two RC components, respectively. The parameter matrices $A_{\mathrm{ECM},k}$, $B_{\mathrm{ECM},k}$, $C_{\mathrm{ECM},k}$, and $D_{\mathrm{ECM},k}$ are shown in Eq. (33) based on Eqs. (18) and (19), in which the term $\theta(\cdot)$ is the simplification of the exponential relationship as in Eq. (34). Based on the identification results in Section 3, the parameters in the matrices are looked up in relation to SOC, in which the term $U_{\mathrm{OCV}}/\mathrm{SOC}(\mathrm{SOC}_k)$ in $C_{\mathrm{ECM},k}$ is the ratio of U_{OCV} and SOC at the present macroscopic SOC.

$$x_{\mathrm{ECM},k} = \left(\mathrm{SOC}_k, U_{po,1,k}, U_{po,2,k}\right)^T \tag{32}$$

$$\begin{cases} A_{\mathrm{ECM},k} = \mathrm{diag}\left(1, \theta(\tau_{\mathrm{po},1}), \theta(\tau_{\mathrm{po},2})\right) \\ B_{\mathrm{ECM},k} = \left(\dfrac{-\Delta t}{Q_{\mathrm{st}} \cdot \eta \cdot 3600}, R_{\mathrm{po},1}\left(1-\theta(\tau_{\mathrm{po},1})\right), R_{\mathrm{po},2}\left(1-\theta(\tau_{\mathrm{po},2})\right)\right)^T \\ C_{\mathrm{ECM},k} = \left(\dfrac{U_{\mathrm{OCV}}}{\mathrm{SOC}}(\mathrm{SOC}_k), -1, -1\right) \\ D_{\mathrm{ECM},k} = -R_{\mathrm{o}} \end{cases} \tag{33}$$

$$\theta(\tau_i) = \exp(-\Delta t/\tau_i) \tag{34}$$

Then the EECM-based SOC estimator is determined with the state vector $x_{\mathrm{EECM},k}$ in Eq. (35), in which $\mathrm{SOC}_{\mathrm{surf},k}$, $U_{\mathrm{DL},1,k}$, $U_{\mathrm{DL},2,k}$, $\Delta\mathrm{SOC}_{1,k}$, and $\Delta\mathrm{SOC}_{2,k}$ are respectively the surface SOC value, the polarization voltages of the double-layer process, and the $\mathrm{SOC}_{\mathrm{surf}}$ offsets due to solid-phase diffusion. The macroscopic SOC is accessible from $x_{\mathrm{EECM},k}$ in Eq. (36). Eq. (37) shows the parameter matrices $A_{\mathrm{EECM},k}$, $B_{\mathrm{EECM},k}$, $C_{\mathrm{EECM},k}$, and $D_{\mathrm{EECM},k}$ based on Eqs. (23)–(27). Different from the ECM, the varying parameters in the EECM matrices are looked up by $\mathrm{SOC}_{\mathrm{surf}}$ value, and the term $U_{\mathrm{OCV}}/\mathrm{SOC}(\mathrm{SOC}_{\mathrm{surf},k})$ in $C_{\mathrm{EECM,k}}$ is the ratio of $U_{\mathrm{OCV}}(\mathrm{SOC}_{\mathrm{surf},k})$ and the present surface SOC $\mathrm{SOC}_{\mathrm{surf},k}$.

$$x_{\mathrm{EECM},k} = \left(\mathrm{SOC}_{\mathrm{surf},k}, U_{\mathrm{DL},1,k}, U_{\mathrm{DL},2,k}, \Delta\mathrm{SOC}_{1,k}, \Delta\mathrm{SOC}_{2,k}\right)^T \tag{35}$$

$$\mathrm{SOC}_k = \mathrm{SOC}_{\mathrm{surf},k} + \Delta\mathrm{SOC}_{1,k} + \Delta\mathrm{SOC}_{2,k} \tag{36}$$

$$\begin{cases} A_{\mathrm{EECM},k} = \begin{pmatrix} 1 & & & & 1-\theta(\tau_{\mathrm{SD},1}) & 1-\theta(\tau_{\mathrm{SD},2}) \\ & \theta(\tau_{\mathrm{DL},1}) & & & & \\ & & \theta(\tau_{\mathrm{DL},2}) & & & \\ & & & \theta(\tau_{\mathrm{SD},1}) & & \\ & & & & & \theta(\tau_{\mathrm{SD},2}) \end{pmatrix} \\ B_{\mathrm{EECM},k} = \left(\dfrac{-\Delta t}{Q_{\mathrm{st}} \cdot \eta \cdot 3600} - k_{\mathrm{SD},1}\left(1-\theta(\tau_{\mathrm{SD},1})\right) - k_{\mathrm{SD},2}\left(1-\theta(\tau_{\mathrm{SD},2})\right), R_{\mathrm{CT},1}\left(1-\theta(\tau_{\mathrm{CT},1})\right), R_{\mathrm{CT},2}\left(1-\theta(\tau_{\mathrm{CT},2})\right),\right. \\ \qquad \left. k_{\mathrm{SD},1}\left(1-\theta(\tau_{\mathrm{SD},1})\right), k_{\mathrm{SD},2}\left(1-\theta\left(\tau_{\mathrm{SD},2}\right)\right)\right)^T \\ C_{\mathrm{EECM},k} = \left(\dfrac{U_{\mathrm{OCV}}}{\mathrm{SOC}}\left(\mathrm{SOC}_{\mathrm{surf},k}\right), -1, -1, 0, 0\right) \\ D_{\mathrm{EECM},k} = -R_{\mathrm{o}} \end{cases} \tag{37}$$

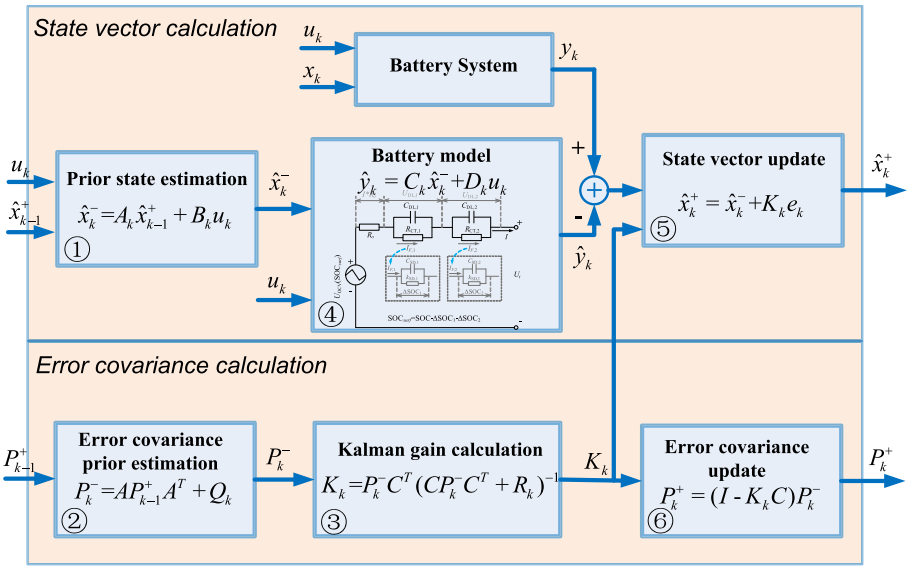

Fig. 24. Schematic of SOC estimation process through extended Kalman filter.

The iteration process of the EKF SOC estimator is shown in Fig. 24 based on the determined state spaces. According to the state $\hat{x}_{k-1}^{+}$ and the error covariance P_{k-1}^{+} of the previous time step as well as the input u_k of the present time point, the SOC estimator derives the present post state estimate $\hat{x}_k^{+}$ and the error covariance estimate P_k^{+}, in which Q_k and R_k are respectively the process and measurement noise covariances and K_k is the calculated Kalman gain. In the iteration process, the prior state $\hat{x}_k^{-}$ and the corresponded model voltage output $\hat{y}_k$ are calculated at first, and the error e_k between the measured and model-estimated voltages is then combined with the Kalman gain K_k to update the state vector.

5.2. Results and comparison

The SOC results of the EKF estimator based on ECM and EECM are compared in this section, in which the experiment data under DST profile is implemented and the sample time Δt is set as 0.1 s. For the initial state x_0, the initial SOC (or SOC_{surf} for the EECM) is determined as 100%, i.e. 30% larger than the real value 70%, and the other voltage terms and SOC_{surf} offsets in the state vector ($U_{po,1,0}$ and $U_{po,2,0}$ for ECM, and $U_{DL,1,0}$, $U_{DL,2,0}$, $\Delta SOC_{1,0}$, and $\Delta SOC_{2,0}$ for EECM) are defined as 0. It is noticed that the SOC updating result in EKF is affected by the initial error covariance P_0 as well as the noise covariances Q_k and R_k, and the corresponded terms in P_0, Q_k, and R_k of the ECM-based and EECM-based estimation systems are hence determined as identical to avoid the influence of noise difference.

Fig. 25 illustrates the SOC estimation results based on the two models, in which the reference SOC is determined by coulomb integration with an accurate initial state. It is shown that both models converge rapidly towards the real SOC to correct the initial

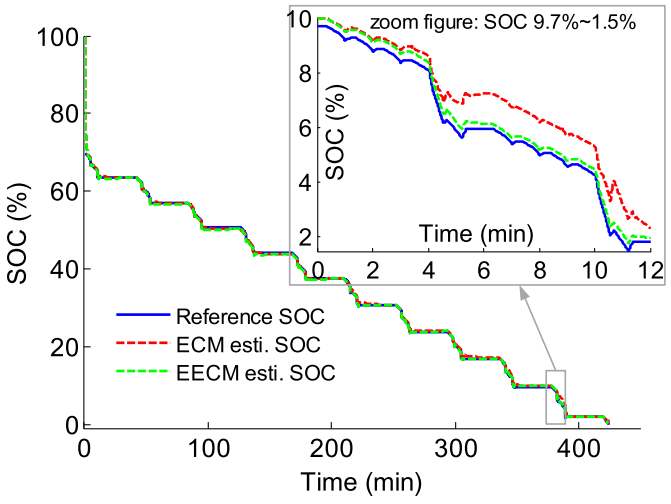

Fig. 25. SOC estimation results comparison through EKF SOC estimator based on ECM and EECM in DST test.

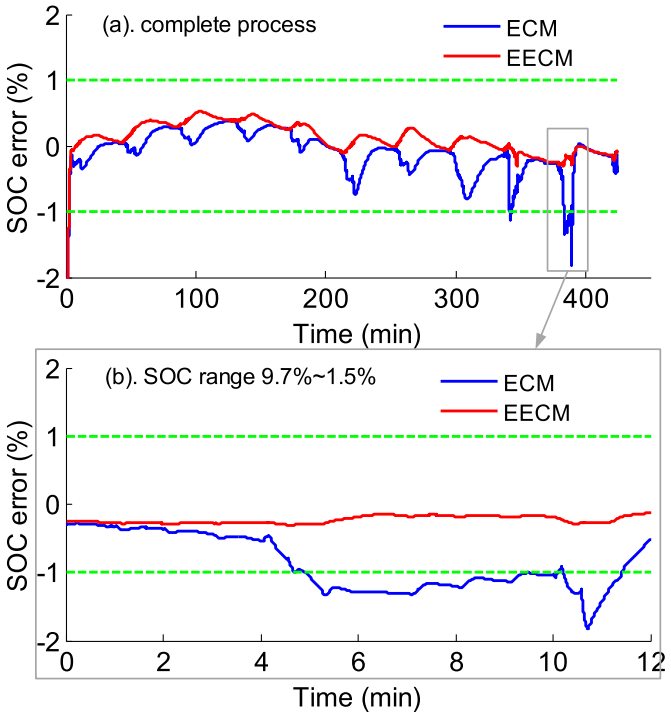

Fig. 26. SOC error comparison of ECM and EECM at different SOC ranges: (a) complete test process; (b) SOC range 9.7%–1.5%.

error, and the SOC errors in a wide SOC range are relatively small. The error increase of ECM-based SOC is noticed in the last test period with SOC 9.7%–1.5%, and the error grows rapidly especially under high discharge rate corresponding to the SOC-rapid-decreasing period in the figure. In contrast, the EECM-based SOC maintains its accuracy in low-SOC area and the performance is little influenced by the discharge rate.

The error between the model-estimated SOC and the real SOC is shown in Fig. 26, in which the error is determined by the real SOC subtracted by the estimated value, and a positive error indicates an underestimation of SOC while a negative error implies SOC overestimation. Both models show good accuracy in a wide SOC area with the SOC error within 1%, and the ECM-based result becomes worse at low SOC with a maximum error of 2% while the EECM always presents very limited errors under 0.5%. Consequently, the EECM helps to improve the estimation accuracy in low-SOC range evidently.

Known from the analysis in Section 4.2, the ECM-based voltage error reaches a maximum of 150 mV in low-SOC area, while the corresponded largest SOC error is 2% and seems not so serious. It is probably because that the SOC–U_{OCV} curve is steeper at low SOC and hence leads to a relatively smaller SOC estimation error with respect to the same voltage error. It seems that the ECM-based SOC error would not influence the E_{RDE} calculation largely, but since the battery model is also used to predict the future terminal voltage in the E_{RDE} determination process as in Eq. (1), the large voltage error together with the SOC error would lead to larger mistakes in E_{RDE} prediction results. The EECM is comparatively with a large advantage in the E_{RDE} and RDR determination.

Additionally, the SOC error based on ECM tends to be negative reflecting that the ECM tends to overestimate the SOC during operation, while a positive error is normally resulted for the EECM indicating underestimation. In the PEV case, the SOC overestimation implies that the battery energy would be exhausted earlier than expected and the vehicle would operate in the limp-home mode before arriving at the destination, which increases the range anxiety of PEV passengers [2]. On the contrary, the SOC underestimation for the EECM indicates more battery energy and more remaining range than expectation, which is relatively safe and could help reduce the users' range anxiety for electric vehicles.

Fig. 27 compares the SOC RMSE under different SOC ranges for the ECM-based and EECM-based EKF estimators, and the RMSE is determined in the periods identical as in Section 4.2. At SOC larger than 20%, the estimation accuracy of both the ECM and the EECM is satisfying with errors under 0.4%. For the SOC under 20% and especially for the lower-than-10% case, the RMSE for the ECM increases largely to a maximum of 1%, while the EECM-based error is still well regulated under 0.4%. As a result, the EECM could evidently enhance the SOC estimation accuracy in low-SOC range.

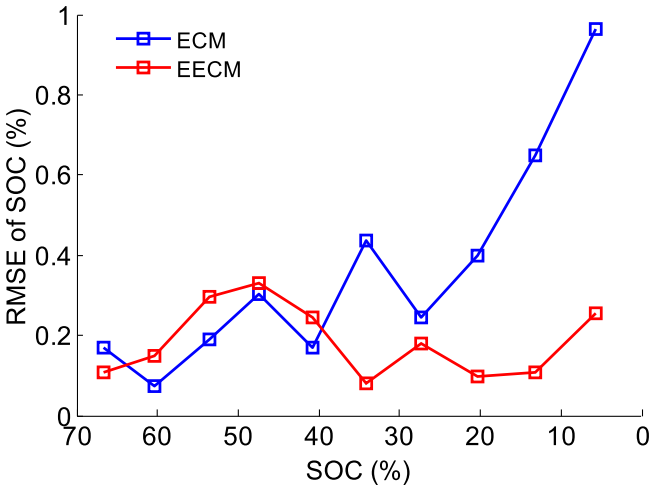

Fig. 27. SOC RMSE comparison of ECM and EECM at different SOCs.

6. Conclusion

In this work, an extended equivalent circuit model (EECM) is presented with enhanced performance in low state-of-charge (SOC) area compared with the traditional equivalent circuit model (ECM). The EECM represents the battery electrochemical process with electrical components, in which two RC components reflect the double layer effect and two one-state elements (DSOCs) indicate the solid-phase diffusion. Different from the ECM which reflects the solid-phase diffusion by polarization voltage, the two DSOC elements in the EECM calculate the difference between the macroscopic SOC and the particle surface SOC (SOC_{surf}), and the obtained SOC_{surf} is then implemented to determine the terminal voltage. The EECM exhibits better nonlinear performance thanks to the SOC_{surf} introduction and could hence provide satisfactory estimation accuracy in low-SOC range.

The effectiveness of the EECM is validated through comparison with the commonly-used two-state ECM on a type of prismatic NCM-G battery. The genetic algorithm is employed in model parameter identification, in which the EECM presents a better fitting result than the ECM at SOC lower than 20%. The voltage estimation accuracy of ECM and EECM is then compared under two types of load profiles in SOC range 0–100%. Under three groups of constant-current discharge pulse profiles (DPP) with 0.5 C, 1 C, and 2 C current rates, the voltage root mean square errors (RMSEs) in low-SOC area are all reduced by more than 50% through the EECM implementation. The error increase under larger current is also smaller for the EECM, indicating its applicability for the high-rate cases. Under DST profiles, the voltage RMSE in low-SOC case is reduced by 64% based on the extended model, implying the effectiveness in dynamic operating conditions. For SOC estimation, the performance of EECM and ECM is discussed through the extended Kalman filtering (EKF) estimator. The result based on the EECM shows a significant advantage in low-SOC range over the traditional ECM, while the EECM-based SOC error is limited under 0.5% in the whole SOC range. Since the model complexity is well controlled, the EECM could be onboard implemented without difficulty to obtain a preciser SOC and voltage estimation result in the entire SOC range, so as to improve the prediction accuracy of the remaining battery energy and the remaining driving range in EV applications. The future work will focus on the possible simplification of the EECM and the model performance validation under different temperatures and aging conditions.

Acknowledgment

This research is funded by the MOST (Ministry of Science and Technology) of China under the contracts of No. 2014DFG71590, the Beijing Science and Technology plan No. Z121100007912001 and the National Support plan 2013BAG16B01, and the MOE (Ministry of Education) of China under the contract of No. 2012DFA81190.

Abbreviations, nomenclature, and subscripts

Abbreviations

Ah	ampere hour
BMS	battery management system
CPE	constant phase element

DPP	discharge pause profile
DST	dynamic stress test
ECM	equivalent circuit model
EECM	extended equivalent circuit model
EIS	electrochemical impedance spectroscopy
EKF	extended Kalman filtering
GA	genetic algorithm
HPPC	hybrid pulse power characterization
LPV	linear parameter varying
NCM	$LiNi_xCo_yMn_{1-x-y}O_2$
PEV	pure electric vehicle
P2DM	pseudo two dimensional model
RDR	remaining driving range
RMSE	root mean square error
SEI	solid electrolyte interface
SOC	state of charge
SPM	single particle model

Nomenclature

A	electrode plate area (m^2)
c_b	bulk average lithium concentration of electrode particle (mol m^{-3})
c_{surf}	lithium concentration at electrode particle surface (mol m^{-3})
$c_{b,0\%}$	bulk average lithium concentration of electrode particle at SOC = 0 (mol m^{-3})
D_s	solid phase diffusion coefficient (m^2 s^{-1})
E_{RDE}	battery remaining discharge energy (Wh)
$\bar{j}$	current density (A m^{-3})
$\bar{j}_{SD}$	solid-phase-diffusional current density (A m^{-3})
$k_{SD,c}$	concentration difference parameter in solid diffusion (mol m^{-3} A^{-1})
k_{SD}	SOC-difference parameters in solid diffusion (m^3 mol^{-1})
Q_{nom}	nominal discharge capacity (Ah)
Q_{st}	standard discharge capacity (Ah)
R_o	Ohmic resistance (Ω)
R_s	radius of spherical particles (m)
SOC_{surf}	surface state of charge (−)
ΔSOC	difference of SOC and SOC_{surf} (−)
U_{OCV}	open circuit voltage (V)
U_0	instantaneous voltage drop in discharge (V)
U_{SEI}	voltage drop on SEI layer (V)
U_t	terminal voltage (V)
δ	electrode or separator thickness (m)
τ	time constant (s)
ε_s	active material volume fraction
$\theta(t)$	exponential relationship: $\exp(-t/\tau)$

Subscripts

Avg	average value
DL	related to double layer
Lim	related to values at discharge voltage limit
N	related to negative electrode
P	related to positive electrode
po	related to polarization terms in ECM
SD	related to solid-phase diffusion
surf	related to values at particle surface

References

[1] T. Franke, J.F. Krems, Transp. Res. A 48 (2013) 109–122.
[2] J. Neubauer, E. Wood, J. Power Sources 257 (2014) 12–20.
[3] C. Truchot, M. Dubarry, B.Y. Liaw, Appl. Energy 119 (2014) 218–227.
[4] X. Hu, S. Li, H. Peng, J. Power Sources 198 (2012) 359–367.
[5] A. Seaman, T.S. Dao, J. McPhee, J. Power Sources 256 (2014) 410–423.
[6] H. He, R. Xiong, H. Guo, S. Li, Energy Convers. Manag. 64 (2012) 113–121.
[7] B.Y. Liaw, G. Nagasubramanian, R.G. Jungst, D.H. Doughty, Solid State Ionics 175 (2004) 835–839.
[8] R. Xiong, F. Sun, X. Gong, C. Gao, Appl. Energy 113 (2014) 1421–1433.
[9] X. Lin, H.E. Perez, S. Mohan, J.B. Siegel, A.G. Stefanopoulou, Y. Ding, M.P. Castanier, J. Power Sources 257 (2014) 1–11.
[10] Y. Hu, S. Yurkovich, Y. Guezennec, B.J. Yurkovich, Control Eng. Pract. 17 (2009) 1190–1201.
[11] M. Dubarry, B.Y. Liaw, J. Power Sources 174 (2007) 856–860.
[12] J. Remmlinger, M. Buchholz, T. Soczka-Guth, K. Dietmayer, J. Power Sources 239 (2013) 689–695.
[13] J. Li, J.K. Barillas, C. Guenther, M.A. Danzer, J. Power Sources 230 (2013) 244–250.
[14] K. Miyatake, T. Abe, Y. Hisamitsu, T. Kinoshita, Y. Shimoida, SAE Technical Paper, 2009, 2009-01-1389.
[15] R. Matthe, L. Turner, H. Mettlach, SAE Int. J. Engines 4 (2011) 1944–1962.
[16] M. Doyle, T.F. Fuller, J. Newman, J. Electrochem. Soc. 140 (1993) 1526–1533.
[17] K. Smith, C.Y. Wang, J. Power Sources 161 (2006) 628–639.
[18] S. Santhanagopalan, R.E. White, J. Power Sources 161 (2006) 1346–1355.
[19] D. Andre, M. Meiler, K. Steiner, H. Walz, T. Soczka-Guth, D.U. Sauer, J. Power Sources 196 (2011) 5349–5356.
[20] S.E. Li, B. Wang, H. Peng, X. Hu, J. Power Sources 258 (2014) 9–18.
[21] D. Di Domenico, A. Stefanopoulou, G. Fiengo, J. Dyn. Sys. Meas. Control 132 (2010), 061302-1–061302–11.
[22] E. Prada, D.D. Domenico, Y. Creff, J. Bernard, V. Sauvant-Moynot, F. Huet, J. Electrochem. Soc. 159 (2012) A1508–A1519.
[23] W. Luo, C. Lyu, L. Wang, L. Zhang, Microelectron. Reliab. 53 (2013) 797–804.
[24] J. Marcicki, A.T. Conlisk, G. Rizzoni, J. Power Sources 251 (2014) 157–169.
[25] E. Barsoukov, D.H. Kim, H.-S. Lee, H. Lee, M. Yakovleva, Yuan Gao, et al., Solid State Ionics 161 (2003) 19–29.
[26] Y. Jia, C.Y. Wang, Electrochim. Acta 107 (2013) 664–674.
[27] S. Santhanagopalan, Q. Guo, P. Ramadass, R.E. White, J. Power Sources 156 (2006) 620–628.
[28] V.R. Subramanian, J.A. Ritter, R.E. White, J. Electrochem. Soc. 148 (2001) E444–E449.
[29] W. Waag, S. Käbitz, D.U. Sauer, Appl. Energy 102 (2013) 885–897.
[30] Idaho National Laboratory, Battery Test Manual for Plug-in Hybrid Electric Vehicles, 2010. http://www.inl.gov/technicalpublications/Documents/4655291.pdf.
[31] J.H. Holland, Adaptation in Natural and Artificial Systems: An Introductory Analysis with Applications to Biology, Control, and Artificial Intelligence, The MIT Press, Massachusetts, 1992.
[32] Y. Zheng, M. Ouyang, L. Lu, J. Li, X. Han, L. Xu, et al., Appl. Energy 111 (2013) 571–580.
[33] W. Waag, D.U. Sauer, Appl. Energy 111 (2013) 416–427.
[34] USABC and DOE National Laboratories Personnel, USABC Battery Test Procedures Manual, 1996. http://avt.inl.gov/battery/pdf/usabc_manual_rev2.pdf.
[35] L. Lu, X. Han, J. Li, J. Hua, M. Ouyang, J. Power Sources 226 (2013) 272–288.
[36] W. Waag, C. Fleischer, D.U. Sauer, J. Power Sources 258 (2014) 321–339.
[37] G. Liu, M. Ouyang, L. Lu, J. Li, X. Han, J. Therm. Anal. Calorim. (2014), http://dx.doi.org/10.1007/s10973-013-3599-9.
[38] M. Dubarry, C. Truchot, B.Y. Liaw, J. Power Sources 219 (2012) 204–216.
[39] G.L. Plett, J. Power Sources 134 (2004) 252–261.
[40] G.L. Plett, J. Power Sources 134 (2004) 262–276.
[41] G.L. Plett, J. Power Sources 161 (2006) 1356–1368.